JOURNAL OF GEOPHYSICAL RESEARCH, VOL. 113, D05101, doi:10.1029/2007JD009255, 2008

Combined use of MODIS, AVHRR and radiosonde data for the estimation of spatiotemporal distribution of precipitable water

N. Chrysoulakis,[1] Y. Kamarianakis,[1] L. Xu,[2] Z. Mitraka,[1] and J. Ding[2]

Received 31 July 2007; revised 22 October 2007; accepted 19 November 2007; published 4 March 2008.

[1] In this paper, the atmospheric precipitable water (PW) was estimated by means of Advanced Very High Resolution Radiometer (AVHRR) thermal channels brightness temperature difference (ΔT), over the broader area of Greece. The AVHRR derived ΔT was calculated in a grid of 5 $\times$ 5 km cells; the corresponding PW value in each grid cell was extracted from Moderate Resolution Imaging Spectroradiometer (MODIS) Level 2 product (near infrared algorithm). MODIS derived PW values were adjusted to the AVHRR overpass time by using PW rates of change. These rates were estimated from time series of radiosonde measurements, provided by four synoptic meteorological stations located in Athens, Thessaloniki, Heraklion and Izmir. Next, to estimate the relationship between adjusted PW and ΔT, a robust linear regression algorithm was applied. Since regression coefficients corresponded to the broader area of Greece, the regression relationship was applied to AVHRR data for the period 2001–2005, to predict the annual and seasonal variability of PW over the study area. Radiosonde derived PW values at the above synoptic stations were used to validate the AVHRR derived PW spatiotemporal distribution. A very good agreement between radiosonde and AVHRR derived PW values was observed since a RMSE of 0.46 cm was calculated using a validation data set that covered a five years period.

Citation: Chrysoulakis, N., Y. Kamarianakis, L. Xu, Z. Mitraka, and J. Ding (2008), Combined use of MODIS, AVHRR and radiosonde data for the estimation of spatiotemporal distribution of precipitable water, *J. Geophys. Res.*, *113*, D05101, doi:10.1029/2007JD009255.

1. Introduction

[2] Water vapor is the principal contributor to the greenhouse effect and plays a key role in our understanding of the Earth's climate. Precipitable water (PW) is the amount of vertically integrated water vapor and can be expressed in g/cm^2, or as the height of an equivalent column of liquid water in cm. Its spatiotemporal distribution is essential in understanding the hydrological cycle, hence it has been adopted as an input variable in climatological studies in global, regional and local scales. PW can be used together with generalized vertical humidity profiles to infer surface dew point. Moreover, it has the potential to support hydrological, biospheric and atmospheric modeling in local and regional scales, since it is widely used in energy budget and evapotranspiration studies. PW is of essential need in atmospheric correction of high spatial resolution satellite data. It is also necessary for the enhancement of the precision of land surface temperature estimates obtained from satellite data by means of split window algorithms, as well as to correct Synthetic Aperture Radar (SAR) interferometric measurements, given that the atmospheric water vapor is a major limitation for high precision Interferometric SAR (InSAR) applications due to its significant impact on microwave signals. The satellite derived high-resolution PW retrievals can be useful in anticipating the distribution of precipitation patterns and in tracking the seasonal and annual variability of PW on regional scales. Thus they are of particular importance for monitoring drought conditions and desertification processes.

[3] PW can be obtained from vertical integration of radiosonde measurements [*Elliott and Gaffen*, 1991; *Gaffen et al.*, 1992; *Bony and Duvel*, 1994; *Cartalis and Chrysoulakis*, 1997; *Chrysoulakis and Cartalis*, 2000; *Chrysoulakis et al.*, 2001]. Radiosonde reports are one of the primary tools for measuring atmospheric water vapor; however, there are some problems associated with their use as atmospheric data. First, the temporal frequency of radiosonde reports is generally limited to two launches per day. Secondly, radiosonde instruments can typically only measure temperature and relative humidity with a precision of about 0.2 K and 3.5%, respectively, resulting errors in PW that range between 5 and 10%. Nevertheless, radiosondes still represent the most accurate means for verifying water vapor amounts [*Motell et al.*, 2002].

[4] PW can also be obtained by analyzing the attenuation that water vapor causes to the radiation signal recorded by a remote sensing radiometer/sounder/radar, or a Global Posi-

[1] Foundation for Research and Technology–Hellas (FORTH), Institute of Applied and Computational Mathematics, Heraklion, Crete, Greece.
[2] Chengdu University of Information Technology, Institute for Space Information and Nonlinear Sciences, Atmospheric Radiation & Satellite Remote Sensing Laboratory, Sichuan, China.

0148-0227/08/2007JD009255$09.00

tioning System (GPS), or a Sun photometer. During the last 20 years, several remote sensing techniques used a variety of spectral regions to estimate PW [*Chesters et al.*, 1983; *Alishouse et al.*, 1990; *Gao and Goetz*, 1990; *Frouin et al.*, 1990; *Smith*, 1991; *King et al.*, 1992, 2003; *Kaufman and Gao*, 1992; *Thome et al.*, 1992; *Guillory et al.*, 1993; *Eck and Holben*, 1994; *Sobrino et al.*, 1994; *Choudhury and Di Girolamo*, 1995; *Uspensky and Scherbina*, 1996; *Knabb and Fuelberg*, 1997; *Halthore et al.*, 1997; *Ottlé et al.*, 1997; *Prince et al.*, 1998; *Barton and Prata*, 1999; *Ottlé and François*, 1999; *Hanssen et al.*, 2001; *Pacione et al.*, 2002; *Chrysoulakis and Cartalis*, 2002; *Johnsen and Kidder*, 2002; *Mallet et al.*, 2002; *Gao and Kaufman*, 2003; *Li et al.*, 2003, 2006; *Jade et al.*, 2005; *Jiménez-Muñoz and Sobrino*, 2005; *Walpersdorf et al.*, 2007; *Schroedter–Homscheidt et. al.*, 2007]. Especially for the thermal infrared spectral region, it has been shown that PW may be estimated from thermal infrared split window channels with an accuracy better than 0.5 cm [*Ottlé et al.*, 1997].

[5] The retrieving of PW using Moderate Resolution Imaging Spectroradiometer (MODIS) near infrared records is based on detecting the water vapor absorption of the reflected solar radiation after it has been transmitted down to the surface, reflected at the surface, and transmitted up through the atmosphere to the sensor. The equivalent total vertical amount of water vapor is derived from a comparison between the reflected solar radiation in the absorption channel, and the reflected solar radiation in nearby non absorption channels [*Gao and Goetz*, 1990; *Frouin et al.*, 1990; *Kaufman and Gao*, 1992; *Thai and Schonermark*, 1998; *Gao and Kaufman*, 2003]. Three near infrared channels located within the 0.94 μm water vapor band absorption region were implemented on MODIS for water vapor sensing. Techniques employing ratios of water vapor absorbing channels centered near 0.905, 0.936, and 0.940 μm with atmospheric window channels at 0.865 and 1.24 μm are used. PW is estimated over areas that have reflective surfaces in the near infrared, such as clear land areas, clouds, and oceanic areas with sun glint [*King et al.*, 2003]. Typical errors for MODIS derived PW over land range between 5% and 10% [*Gao and Kaufman*, 2003]. The sources of errors for PW retrievals from near infrared channels include uncertainties in the spectral reflectance of the surface, sensor radiometric and spectral calibrations, pixel registration between several channels, atmospheric temperature and moisture profiles, and the amount of haze [*Kaufman and Gao*, 1992; *Bouffies et al.*, 1997].

[6] A number of algorithms have been proposed to derive PW from Advanced Very High Resolution Radiometer (AVHRR) thermal infrared observations [*Dalu*, 1986; *Jedlovec*, 1990; *Kleespies and McMillin*, 1990; *Goward et al.*, 1994; *Prince and Goward*, 1995; *Andersen*, 1996; *Roger and Vermote*, 1998]. These methods can be classified into four main categories: The simple split-window of thermal channels [*Dalu*, 1986], the variance ratio [*Jedlovec*, 1990], the regression slope [*Goward et al.*, 1994], the covariance-variance method [*Harris and Mason*, 1992] and the look-up table approach [*Czajkowski et al.*, 2002]. The impact of satellite viewing angle in PW estimation has been discussed by *Dalu* [1986], *Sobrino et al.* [1994], *Choudhury et al.* [1995], *Ottlé et al.* [1997], *Prince et al.* [1998] and *Motell et al.* [2002]. It should be noted that emissivity over land surfaces presents a significant complication in interpreting split window temperature differences, however accuracies of better than 0.5 cm water can be achieved [*Dalu*, 1986; *Justice et al.*, 1991; *Eck and Holben*, 1994].

[7] Let T_4 and T_5 denote the brightness temperatures of AVHRR channels 4 and 5, respectively. Analysis of the split window temperature differences $\Delta T = T_4 - T_5$, for land surfaces in several different climatic regions with differing soil compositions and vegetative covers, revealed a linear relationship between ΔT and PW [*Eck and Holben*, 1994; *Choudhury et al.*, 1995]. The accuracy of the split window technique is uncertain in arid environment during daytime due to strong near-surface air temperature gradient [*Choudhury and Di Girolamo*, 1995]. Provided that the channels 4 and 5 radiances are accurately calibrated [*Goodrum et al.*, 2001], the AVHRR split window technique of PW estimation has the potential to provide consistent estimates of PW for a multiyear database. This technique can be referenced to a given year of independent (satellite, radiosonde, Sun photometer, GPS etc.) data or analyzed PW fields and thus provide consistent multiyear estimates for each location. As discussed by *Choudhury et al.* [1995], spatial and temporal changes of ΔT and PW can also be associated with the changes of land surface characteristics and hence the emissivity. The high correlations found by *Eck and Holben* [1994] suggest that the spatial variation of emissivity, associated with significant changes of surface characteristics, can have a higher impact on the PW-ΔT relationship than temporal variations at a specific location.

[8] In this paper the MODIS precipitable water Level-2 product is related to the AVHRR derived ΔT after an adjustment that takes into account the time lag between the time of the two satellite passes. The adjustment used radiosonde derived PW rates of change collected at four synoptic meteorological stations (Athens, Thessaloniki, Heraklion and Izmir). All spatial calculations were performed in a grid of 5 $\times$ 5 km cells over the study area. Preliminary data investigation revealed a linear relationship between adjusted PW and ΔT; to eliminate the effect of outlying measurements, the parameters that characterize this relationship were estimated via a robust regression procedure. The PW–ΔT relationship was applied to AVHRR data to provide multiyear PW spatial distributions and was validated against radiosonde derived PW time series at the abovementioned synoptic stations. AVHRR data acquired during the mid month of each season (January, April, July, and October) for the time period 2001–2005 were used, therefore the seasonal variability of PW was also assessed.

2. Study Area and Data Sets

2.1. The Study Area

[9] The study area is the broader area of Greece. In Figure 1, the location of the four radiosonde stations (Athens, Thessaloniki, Heraklion and Izmir) is highlighted in the study area and a grid comprised by 5 $\times$ 5 km cells is superimposed. The PW–ΔT relationship was calibrated at 5 $\times$ 5 km cell level; for this reason the 1 $\times$ 1 km AVHRR and MODIS derived data were spatially aggregated in 5 $\times$ 5 km cells. In particular, ΔT was estimated at AVHRR pixel level and the mean value in each grid cell was computed.

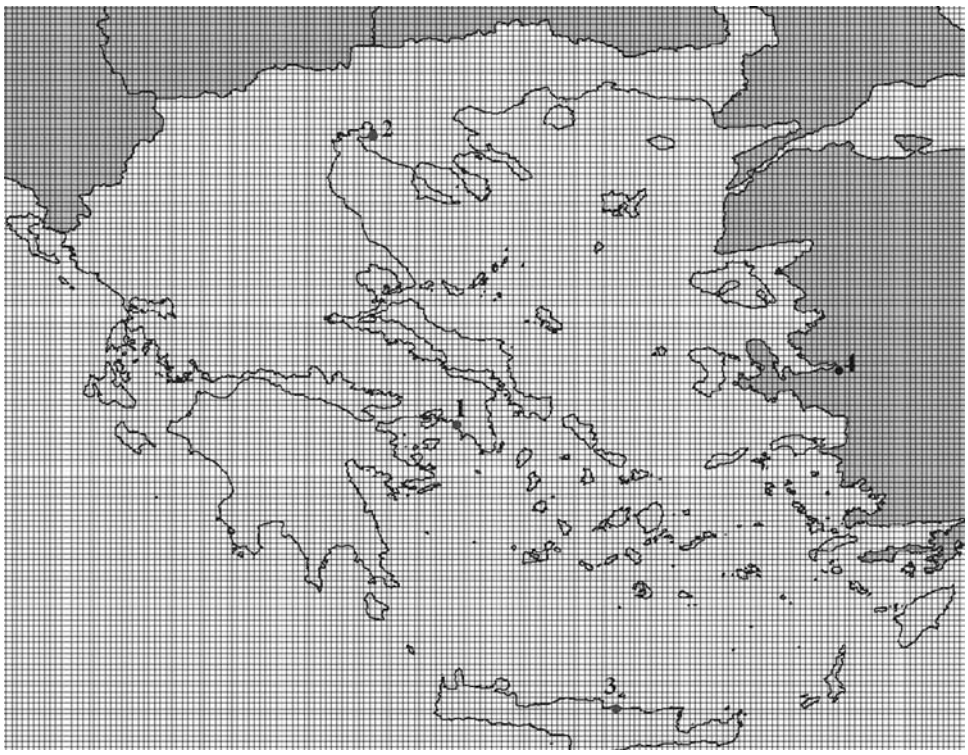

Figure 1. The study area. The MODIS derived PW and the AVHRR derived ΔT were spatially averaged in 5×5 km. For this reason a grid of 5×5 km cells was developed (Projection: Geographic-WGS 84). For each of the 15 data sets shown in Table 1, only cloud free cells over land were used. The location of Athens (1), Thessaloniki (2), Heraklion (3) and Izmir (4) meteorological stations is shown.

[10] As it will be explained later, near nadir AVHRR acquisitions over the study area were used, therefore the effect of satellite zenith angle was ignored. Likewise the PW values extracted at 1×1 km level from the MODIS Level 2 product were aggregated in 5×5 km cells. To calibrate the PW$-\Delta$T relationship, 15 MODIS and AVHRR acquisitions were used.

[11] Table 1 displays the respective dates and overpass times of both Tearra/MODIS and NOAA16/AVHRR. Moreover, Table 1 presents observations of the meteorological horizontal visibility at 0.55 μm at the above synoptic stations. These observations are part of the global synoptic weather reports received via the Global Telecommunication System (GTS) at the European Center for Medium range Weather Forecast (ECMWF). As depicted in the table, visibility values are grater than 10 km in all cases. Therefore it was considered that the atmospheric aerosol content was low and thus the effect of aerosols in thermal infrared radiation absorption was ignored.

2.2. The MODIS Data

[12] The MODIS radiometer has 36 channels that cover the spectral region between 0.4 and 15 μm. Five near infrared channels centered at 0.865, 0.905, 0.936, 0.940, and 1.240 are used for PW sensing. The channels at 0.865 and 1.24 μm positioned to avoid atmospheric gaseous absorption are used for remote sensing of vegetation and clouds. The channels at 0.936, 0.940, and 0.905 μm are water vapor absorption channels with decreasing absorption coefficients. The strong absorption channel at 0.936 μm is most useful for dry conditions, while the weak absorption channel at 0.905 mm is most useful for very humid conditions, or low solar elevation [*Gao and Kaufman*, 2003].

[13] The MODIS Level 2 precipitable water product consists of column water vapor amounts. The results of the near infrared retrieval algorithm over land were used in this study; this algorithm [*Gao and Kaufman*, 2003] is applied over clear land areas of the globe and above clouds over both land and ocean during daytime. Over clear ocean areas, water vapor estimates are provided over the extended glint area. The Level 2 data are generated at the 1-km spatial resolution of MODIS using the near-infrared algorithm during the day. For this work, the Terra/MODIS PW retrievals for the study area for 15 days of October 2003, January, April and July 2004 (Table 1) were selected; the selection criteria are explained in section 3.1. These Terra data (collection 5) were available from the Level 1 and Atmosphere Archive and Distribution System [*LAADS*, 2007].

2.3. The AVHRR Data

[14] Records of AVHRR onboard NOAA 16 acquired over the study area for the five year period 2001–2005 (for the months January, April, July and October) were used to derive the spatiotemporal distribution of PW. The AVHRR is a five channel instrument, with three of the spectral channels located in the visible, near-infrared and mid infrared regions of the spectrum, while the remaining two are located in the thermal infrared with effective wavelengths centered around 10.8 μm (channel 4), and 12 μm (channel 5). It has the same spatial characteristics with previous versions of AVHRR; spatial resolution of 1.1 km at nadir and swath coverage of 2700 km. For the present

Table 1. Dates and Overpass Times of Tearra/MODIS and NOAA16/AVHRR Acquisitions Used in This Study[a]

Date	Terra/MODIS Pass Time, UTC	NOAA16/AVHRR Pass Time, UTC	Pass Time Difference	Meteorological Horizontal Visibility (0.55 μm) at 12:00 UTC, km			
				Athens	Thessaloniki	Heraklion	Izmir
2 Oct 2003	09:30	13:00	3:30	10	15	15	15
4 Oct 2003	09:20	12:35	3:15	10	10	20	15
12 Oct 2003	08:30	12:45	4:15	20	10	15	15
22Oct 2003	09:05	12:35	3:30	10	10	25	15
7 Jan 2004	08:35	12:05	3:30	15	10	15	15
17 Jan 2004	09:15	11:55	3:40	15	20	20	15
25 Jan 2004	10:00	12:05	2:05	15	10	15	15
6 Apr 2004	09:15	12:50	3:35	10	10	20	15
16 Apr 2004	09:50	12:35	2:45	15	10	20	15
23 Apr 2004	09:10	12:55	3:45	15	10	15	15
29 Apr 2004	09:20	13:30	4:10	12	10	20	15
1 Jul 2004	09:25	13:15	3:50	15	15	20	15
7 Jul 2004	09:35	13:50	4:15	15	10	20	15
8 Jul 2004	08:40	13:35	4:55	15	20	15	15
9 Jul 2004	09:25	13:25	4:00	15	15	20	15

[a]The pass time difference (Δt) is also presented, as well as the observations of the meteorological horizontal visibility at 0.55 μm at four representative meteorological stations: Athens, Thessaloniki, Heraklion and Izmir (Figure 1). Its values are grater than 10 km in all cases, therefore we can consider that the atmospheric aerosol content is low and thus the effect of aerosols in thermal infrared radiation absorption can be ignored.

study, the AVHRR data were available from both NOAA Satellite Active Archive [CLASS, 2005] and the HRPT ground receiving station of FORTH (Foundation for Research and Technology-Hellas). For the PW-ΔT relationship calibration, data corresponding to the 15 days presented in Table 1 were used.

2.4. The Radiosonde Data

[15] Upper air data is reported up to four times per day at the synoptic hours of 00:00, 06:00, 12:00 and 18:00 UTC. The frequency varies widely between countries and stations. Standard practice states that all measurements in the profile are attributed to the nominal hour of the ascent: this is the time the radiosonde reaches 100 hPa. It takes approximately an hour for the balloon to rise to this level, hence the radiosondes are released one hour before the synoptic times. The radiosonde takes measurements at intervals of approximately 2 s; high resolution data files contain all such data. The standard resolution data files contain measurements taken at particular levels of the atmosphere.

[16] Radiosonde data consist of height profiles for pressure, temperature and dew point. Radiosondes are expected to produce PW with an uncertainty of 0.1–0.2 cm, which is considered to be the accuracy standard of PW for meteorological applications [*Met Office*, 2006]. Radiosonde measurements at four synoptic stations were used in this study: Athens (37.90 N, 23.73 E), Thessaloniki (40.52 N, 22.97 E), Heraklion (35.33 N, 25.18 E) and Izmir (38.43 N, 27.17 E). The data (daily pressure, temperature and humidity measurements at several levels of radiosonde rising for 00.00 and 12.00 UTC) for the study period (2001–2005) were obtained from the UK Meteorological Office. The accuracy of radiosonde measurements is ±0.5 hPa for pressure, ±0.2 K for temperature and ±2 % for relative humidity [*Met Office*, 2006].

3. Methodology

3.1. Overview

[17] Theoretical analysis proposes an almost linear relationship between PW and ΔT, with slope and intercept being determined by the surface emissivity. Spectral variation of emissivity is found to be the major factor that causes deviation of the intercept from a nearly zero value [*Choudhury et al.*, 1995]. Assuming that the surface is Lambertian, the land-atmosphere system is spatially homogeneous, and a first-order Taylor's series expansion of the Planck's function is a good approximation, a split window algorithm can be applied to AVHRR thermal infrared channels [*Choudhury and Di Girolamo*, 1995]. As it has been shown in past studies [*Dalu*, 1986; *Justice et al.*, 1991; *Eck and Holben*, 1994; *Choudhury and Di Girolamo*, 1995; *Czajkowski et al.*, 2002], if the radiative transfer equation is linearized, the PW is proportional to the difference between the two AVHRR thermal channels brightness temperature.

[18] The linearity of the PW–ΔT relationship was tested using a radiative transfer model for different ground emissivities. The Santa Barbara DISORT Atmospheric Radiative Transfer (SBDART) model [*Ricchiazzi et al.*, 1998] was used. SBDART was run for representative latitude and longitude for the study area (38° N, 23.5° E), for a time around the NOAA 16 pass (13:00 UTC), using several land cover types (emissivities) such as Water, Vegetation, Brown Sandy Loam, White Gypsoum Dune Sand and Urban Asphalt, for different troposphere aerosols load (zero aerosol, aerosol optical depth equal to 1 and 3). The longwave radiation recorder by AVHRR channel 4 and 5 was simulated by SBDART for PW values from 0.5 to 2.5, which combined with the aforementioned land cover types and aerosol loadings provided several scenarios for SBDART runs. ΔT was calculated for each case as the difference of the simulated temperature in AVHRR channels 4 and 5. The temperature in each of these channels was derived from the simulated by SBDART radiance using the Planck equation for blackbody. The calculations based on SBDART simulations are shown in Table 2. The linearity of PW –ΔT relationship is evident in Figure 2, where PW versus ΔT scatterplots based on SBDART simulations are presented: (a) PW–ΔT scatterplot for 5 land cover types for aerosol free atmosphere; (b) and (c) PW–ΔT scatterplots for 5 land cover types for tropospheric aerosol with aerosol optical

Table 2. ΔT for Different Combinations of PW, Aerosol Loads and Land Cover (Emissivity) Types as Resulted From SBDART Simulations

Land Cover	PW, cm	ΔT, K		
		No Aerosols	Tropospheric Aerosols $\tau = 1$	Tropospheric Aerosols $\tau = 3$
Vegetation	0.5	1.147	1.0878	0.5159
	1	1.6238	1.5699	0.8991
	1.5	2.0913	2.0445	1.3191
	2	2.5386	2.496	1.7717
	2.5	2.9486	2.981	2.6358
Water	0.5	1.147	1.0878	0.5159
	1	1.6239	1.5699	0.8991
	1.5	2.0913	2.0445	1.3191
	2	2.5385	2.496	1.7716
	2.5	2.9486	2.981	2.6358
Brown Sandy Loam	0.5	0.8043	0.7673	0.3503
	1	1.2247	1.1939	0.6815
	1.5	1.6652	1.6377	1.064
	2	2.1148	2.0905	1.4975
	2.5	2.5523	2.5948	2.3507
White Gypsum Dune Sand	0.5	0.8702	0.8272	0.3808
	1	1.3046	1.2678	0.7229
	1.5	1.7531	1.7196	1.115
	2	2.2026	2.1744	1.5528
	2.5	2.6367	2.6752	2.4103
Urban Asphalt	0.5	0.6734	0.6398	0.257
	1	1.1056	1.0731	0.5895
	1.5	1.5566	1.528	0.9837
	2	2.0224	1.997	1.4286
	2.5	2.4746	2.5216	2.2929

depths $\tau = 1$ and $\tau = 3$, respectively; (d) linear fittings using all land cover types for each aerosol case separately.

[19] This split-window technique is not a universal solution to PW retrieval due to the dependence of the difference ΔT on air temperature and surface characteristics. Linear relationships characterized by different coefficients are expected to hold in different locations. The coefficients of the linear relationship between PW and ΔT are site specific and can be derived as an output from a radiative transfer model, or as observational data at each location. In this study, MODIS derived PW were used as an independent data set, adjusted for the time lag between the time of Terra/MODIS and NOAA16/AVHRR overpasses. Radiosonde data were used for this adjustment as it is described in section 3.5. More specifically, if the AVHRR acquisition over the study area is performed at $t = t_0$, the PW at this time, $PW(t_0)$, can be estimated as linear function of ΔT:

$$PW(x, y, t_0) = a\Delta T(x, y, t_0) + b \quad (1)$$

where,

- $PW(x, y, t_0)$ is the total column precipitable water in the (x, y) cell of the grid at AVHRR acquisition time (t_0),
- x, y are the coordinates of the center of the cell,
- a and b are coefficients that need to be estimated for the study area,
- $\Delta T = T_4 - T_5$ is the brightness temperatures for channels 4 and 5 in the (x, y) cell. The data for AVHRR channels 4 and 5 are given in digital numbers (Level 1b format), which are converted to radiance at the sensor and finally to brightness temperatures to the allowable accuracy of 0.5 K [*Goodrum et al.*, 2001].

[24] It is noted that the uncertainty in inferring PW from radiosonde is around 5% [*Eck and Holben*, 1994]. However, the uncertainty in estimating PW using AVHRR records for the time of MODIS overpass is probably larger due to temporal variations in PW amount. By a Taylor's series expansion of PW about the time t_0 we obtain:

$$PW(x, y, t) = PW(x, y, t_0) + \Delta t \frac{\partial PW(x, y, t_0)}{\partial t} \quad (2)$$

where,

- PW(x, y, t) is the PW in the (x, y) cell at MODIS acquisition time (t),
- x, y are the coordinates of the center of the cell,
- $PW(x, y, t_0)$ is the PW value at the same location at the AVHRR acquisition time,
- $\Delta t = t - t_0$ is the time difference between MODIS and AVHRR passes,

[29] $\frac{\partial PW(x,y,t_0)}{\partial t}$ is the partial derivative of PW with respect to time at the (x, y) location, being evaluated at $t = t_0$. It represents the rate of change of PW in a grid cell with coordinates x and y.

[30] Therefore the MODIS derived PW can be related to the AVHRR derived ΔT as:

$$PW(x, y, t) - \Delta t \frac{\partial PW(x, y, t_0)}{\partial t} = a\Delta T(x, y, t_0) + b \quad (3)$$

[31] The term $PW(x, y, t) - \Delta t \frac{\partial PW(x,y,t_0)}{\partial t}$ represents an estimation of the actual precipitable water during the AVHRR acquisition time called the adjusted precipitable water (PW*). PW* was computed by combining MODIS derived PW with radiosonde derived PW rates of change over the study area. The latter was derived by spatial interpolation using the PW rates of change calculated at the synoptic stations of Athens, Thessaloniki, Heraklion and Izmir. Consequently, for a grid cell with coordinates x and y, the equation (3) can be written as:

$$PW^*(x, y, t_0) = a\Delta T(x, y, t_0) + b \quad (4)$$

[32] The coefficients a and b in (4) can be estimated by linear regressions of PW*versusΔT. In this study, the estimation of the coefficients a and b was based on MODIS, AVHRR and radiosonde data acquired during the selected days of 2003 and 2004 (Table 1). The selection criteria for these days were: a) As much cloud free land area as possible and b) near nadir NOAA16/AVHRR acquisitions over the study area. We performed a selection of cloud free (in both

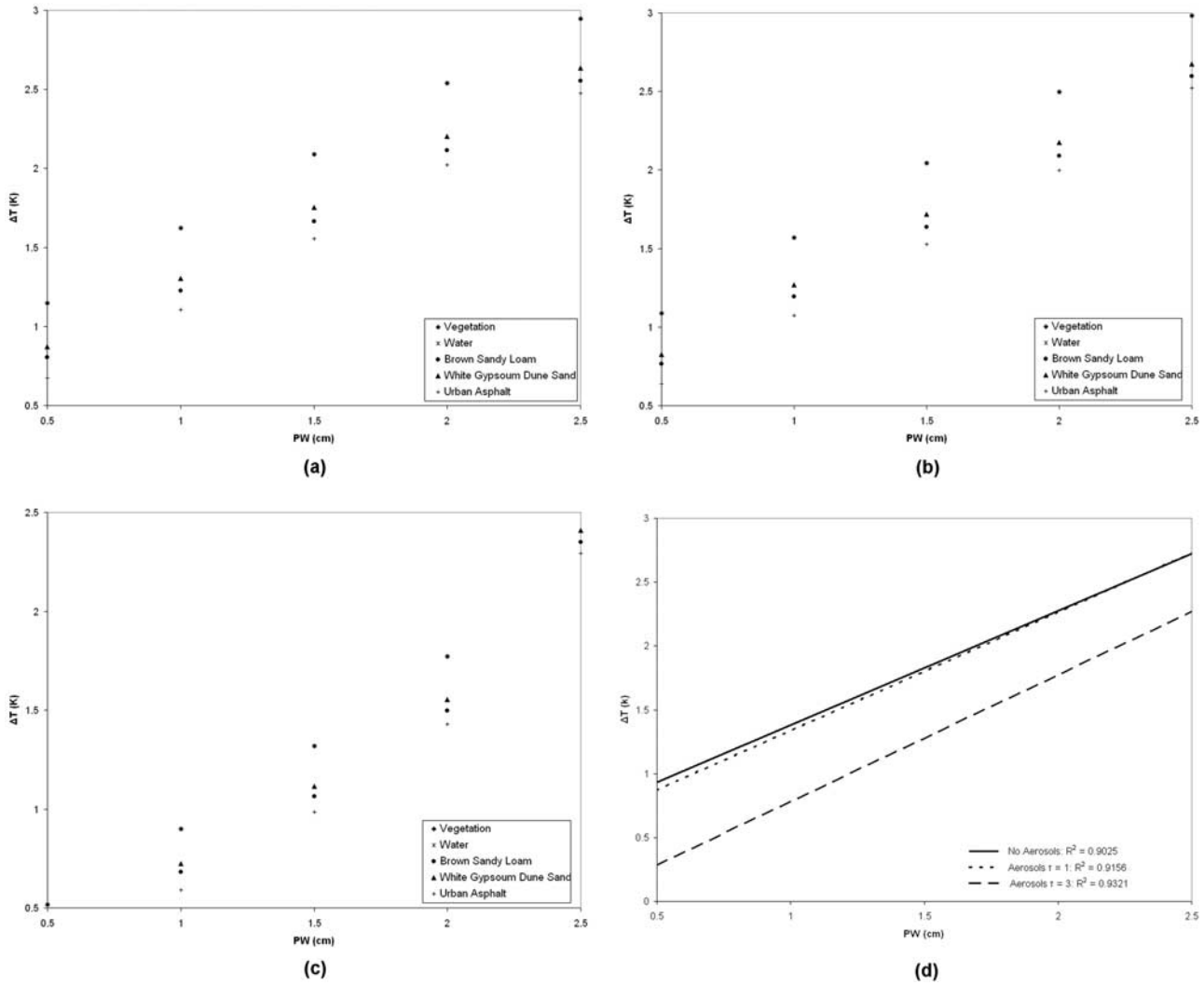

Figure 2. PW versus ΔT scatterplots based on SBDART simulations (Table 2): (a) PW$-\Delta T$ scatterplot for 5 land cover types for aerosol free atmosphere; (b) and (c) PW$-\Delta T$ scatterplots for 5 land cover types for tropospheric aerosol with aerosol optical depths $\tau = 1$ and $\tau = 3$, respectively. The linear PW$-\Delta T$ relationship and the effect of emissivity on intercept is evident in all cases. (d) Linear fittings using all land cover types for each aerosol case separately. The linear PW$-\Delta T$ relationship is evident from the high R^2 values. The effect of atmospheric aerosol on both slope and intercept is also evident.

MODIS and AVHRR images) cells corresponded to land aiming to have as much cells of the same location as possible (at least for the same month).

[33] As shown in Table 1, the aerosol concentration was low, since meteorological horizontal visibilities greater than 10 km are observed in all cases. Moreover, the values of horizontal visibilities in Table 1, suggested that there was no Saharan dust episode, thus it was assumed that the aerosol haze was composed predominately of small size particles relative to the long wavelength thermal infrared channels of AVHRR, having a small effect in observed radiances [*Choudhury et al.*, 1995].

[34] The estimated PW*$-\Delta T$ relationship was applied to AVHRR data to provide PW spatial distributions for the period 2001–2005 (for January, April, July, and October) and it was validated using radiosonde derived PW time series at the synoptic stations of Athens, Thessaloniki, Heraklion and Izmir. A very good agreement was observed as it is described in section 3.7.

3.2. Radiosonde Derived Precipitable Water

[35] The radiosonde measurements (pressure, temperature and dew point temperature) were used to estimate the rate of change of PW, which was necessary for the calibration procedure. These measurements also provided a set of time series that was used as an independent data set for validation. The PW was estimated using the approach described by *Cartalis and Chrysoulakis* [1997] and by *Chrysoulakis and Cartalis* [2000]: The atmospheric column was divided in several layers (according to the radiosonde sampling rate) and PW was estimated by summing the water vapor mixing ratio in each atmospheric layer multiplied by the depth (pressure difference between top and bottom) of the layer. The water vapor mixing ratio was estimated as a function of

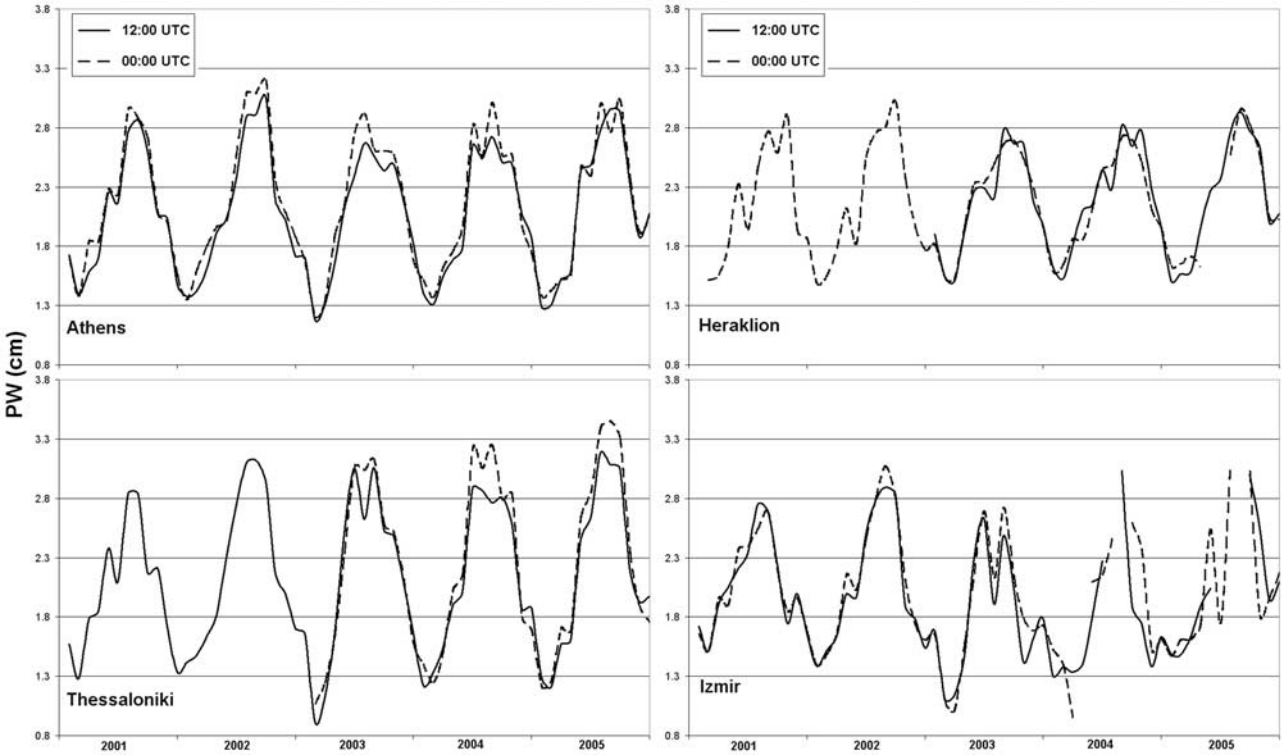

Figure 3. Monthly mean PW values as calculated using 00:00 UTC and 12:00 UTC radiosonde measurements at synoptic stations of Athens (37.90 N, 23.73 E), Thessaloniki (40.52 N, 22.97 E), Heraklion (35.33 N, 25.18 E) and Izmir (38.43 N, 27.17 E). The interanually variability of the atmospheric humidity is evident in all cases (00:00 UTC measurements for Thessaloniki for 2001–2002, 12:00 UTC measurements for Heraklion for 2001–2002, as well as some 00:00 UTC and 12:00 UTC values for Izmir, for 2004 and 2005 are missing).

the moist air density which in turn was estimated using the relative humidity and the saturation water vapor pressure values. The relative humidity was calculated using the radiosonde derived temperature and dew point temperature measurements [*Iribarne and Godson*, 1981]. Finally, the saturation water vapor pressure in each layer was calculated from the radiosonde temperature measurements using the Magnus' formula [*Iribarne and Godson*, 1981].

[36] It should be noted that temperature and/or dew point temperature measurements at some heights were missing. Both temperature and dew point temperature were considered functions of pressure. To fill missing values, a linear interpolation method was applied separately for each radiosonde (00:00 UTC or 12:00 UTC) at each synoptic station. Radiosondes with more than 50% missing values (especially in lower atmospheric layers) were not included in the analysis. Finally, the radiosonde derived PW values were filtered to remove outliers, which resulted either due to missing temperature or humidity values at specific heights, or due to interpolation or extrapolation errors.

3.3. MODIS Derived Precipitable Water

[37] As noted before, MODIS PW retrievals for October 2003, January, April, and July 2004 were used [*LAADS*, 2007]. The data were available as images (PW scenes from collection 5) in Hierarchical Data Format (HDF). A Matlab script was developed to read the HDF files, to extract the PW values for each pixel and to assign a flag value to all the cloudy pixels of each PW scene. The original HDF files were modified using the Software Library and Utilities for National Center for Supercomputing Applications (NCSA) HDF, through Matlab's user interface [*NCSA*, 2003]. A scale factor was included to convert the scaled integer values to PW values (cm); integer values were scaled using the scale factor included in each HDF file.

[38] Information about cloud cover was included in HDF format. A cloud mask in bit-level representation provided criteria that guide one to decide if a pixel of the PW scene was cloudy or not. A pixel can be classified as cloudy, 66% probably clear, 95% probably clear and 99% probably clear. In this study, pixels that considered being less than 5% cloudy were used.

[39] Navigation parameters were also included in HDF format; these parameters were used to correct the panoramic distortion and to project each PW scene in a common projection system (Geographic with WGS84 ellipsoid and datum). The nearest neighbor resampling method was used to geometrically correct the PW scenes. Consequently, the MODIS derived PW was transformed to geometrically corrected scenes at 1 km spatial resolution. Real PW values were assigned to non cloudy pixels whereas the cloudy pixels were masked. Finally, all scenes were spatially averaged to the 5×5 km cell grid covering the study area. It should be noted that the spatial averaging was performed

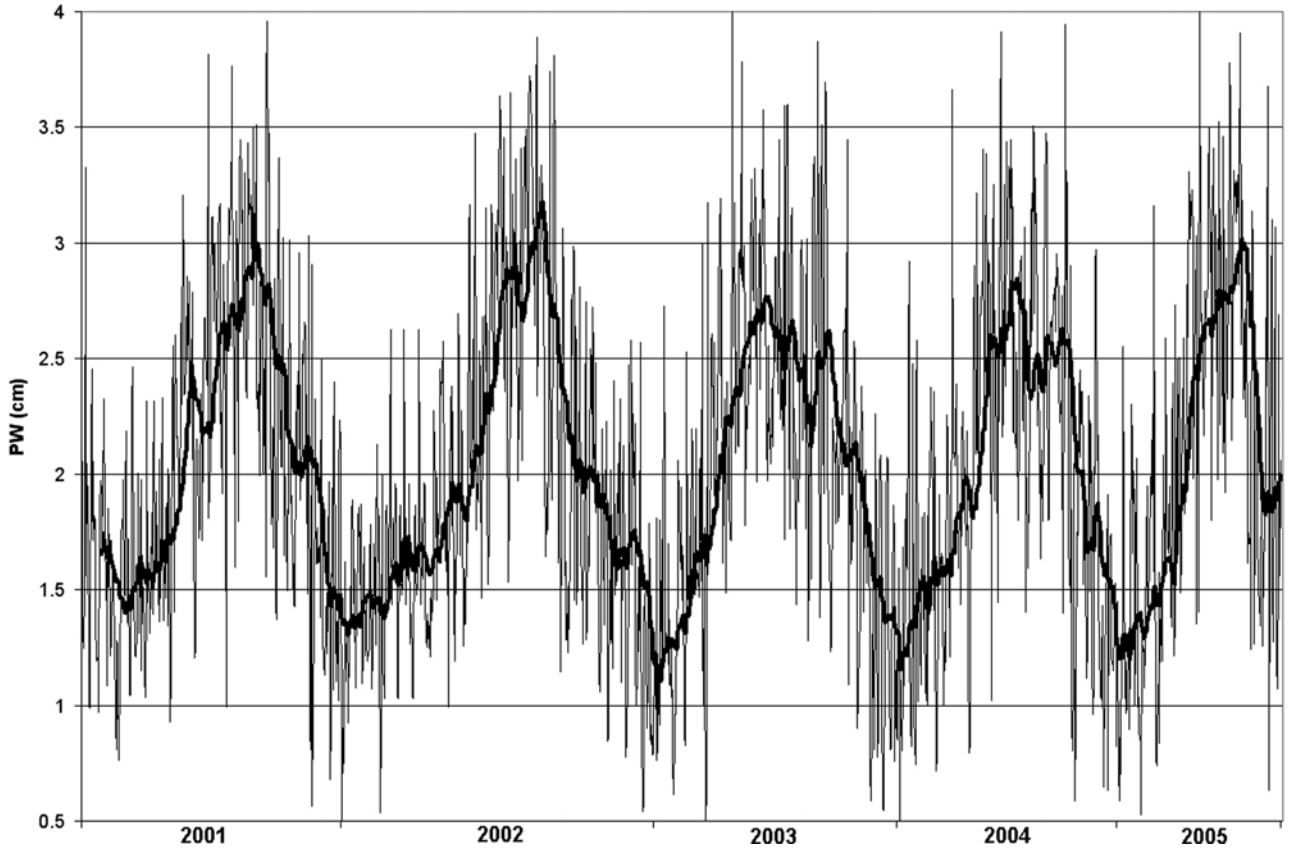

Figure 4. Daily PW values calculated using the 12:00 UTC radiosonde measurements at Athens synoptic station (37.90 N, 23.73 E) for the 5-year period 2001–2005. A moving average (with 1 month period) has been superimposed (bold curve), which reveals the interannual variability of PW.

if all pixels corresponding to each grid cell were non-cloudy. If one or more cloudy pixels were included, a flag value was assigned to the respective cell.

3.4. AVHRR Derived Brightness Temperature Difference

[40] Standard pre-processing steps were employed to convert the raw AVHRR records to calibrated values. The calibration procedure was based on the conversion of digital numbers of each image to radiance at the sensor values for visible and near infrared channels (channels 1 and 2) and to brightness temperature values for the thermal infrared channels (channels 3, 4 and 5) with the use of the non-linear conversion equations given in the NOAA KLM Polar Orbiter Data Users Guide [*Goodrum et al.*, 2001]. The intercept and gain for each AVHRR channel, as well as the parameters related to the central wave number and the constants needed to parameterize the calibration equations were extracted from the NOAA Level 1b header of each image file. The platform flight altitude was also extracted from the same source and it was used for the geometric correction and the correction of the panoramic distortion in calibrated AVHRR images. The geometric correction was fine-tuned manually using a limited number of Ground Control Points (GCPs). The standard NOAA projection system (Geographic with ellipsoid and datum WGS 72) was used. The selection of GCPs was rather easy due to the high land–sea contrast over the Aegean Sea, where several small islands exist. The images were finally reprojected to the standard MODIS projection system in order to have all the data sets in the same system. The nearest neighborhood resampling method was used in all cases.

[41] To derive the spatial distribution of ΔT at 5×5 km level for the mid month of each season of the study period with accuracy, a cloud mask filter proposed by *Chrysoulakis and Cartalis* [2003] was used to detect cloudy pixels. Accordingly, ΔT was calculated at AVHRR pixel level (1.1 km) for non cloudy pixels. ΔT values were spatially averaged at the 5×5 km level assigning a mean ΔT value in each grid cell. As for the MODIS data, spatial averaging was performed if all pixels corresponding to each grid cell were non cloudy. The above steps were repeated for almost all days (one near nadir acquisition of NOAA 16 per day) of the months January, April, July and October of the time period 2001–2005. Days with unsuccessful acquisitions over the study area were not included in the analysis.

3.5. Estimation of the Rate of Change of Precipitable Water

[42] The term $\frac{\partial PW(x,y,t_0)}{\partial t}$ in equation (3) was estimated using radiosonde derived PW time series at the synoptic stations of Athens, Thessaloniki, Heraklion and Izmir. Radiosonde derived PW values measured before (usually at 00:00 UTC) and after (usually at 12:00 UTC) the MODIS acquisition were used to calculate the rate of change of PW at the locations of these synoptic stations. These values

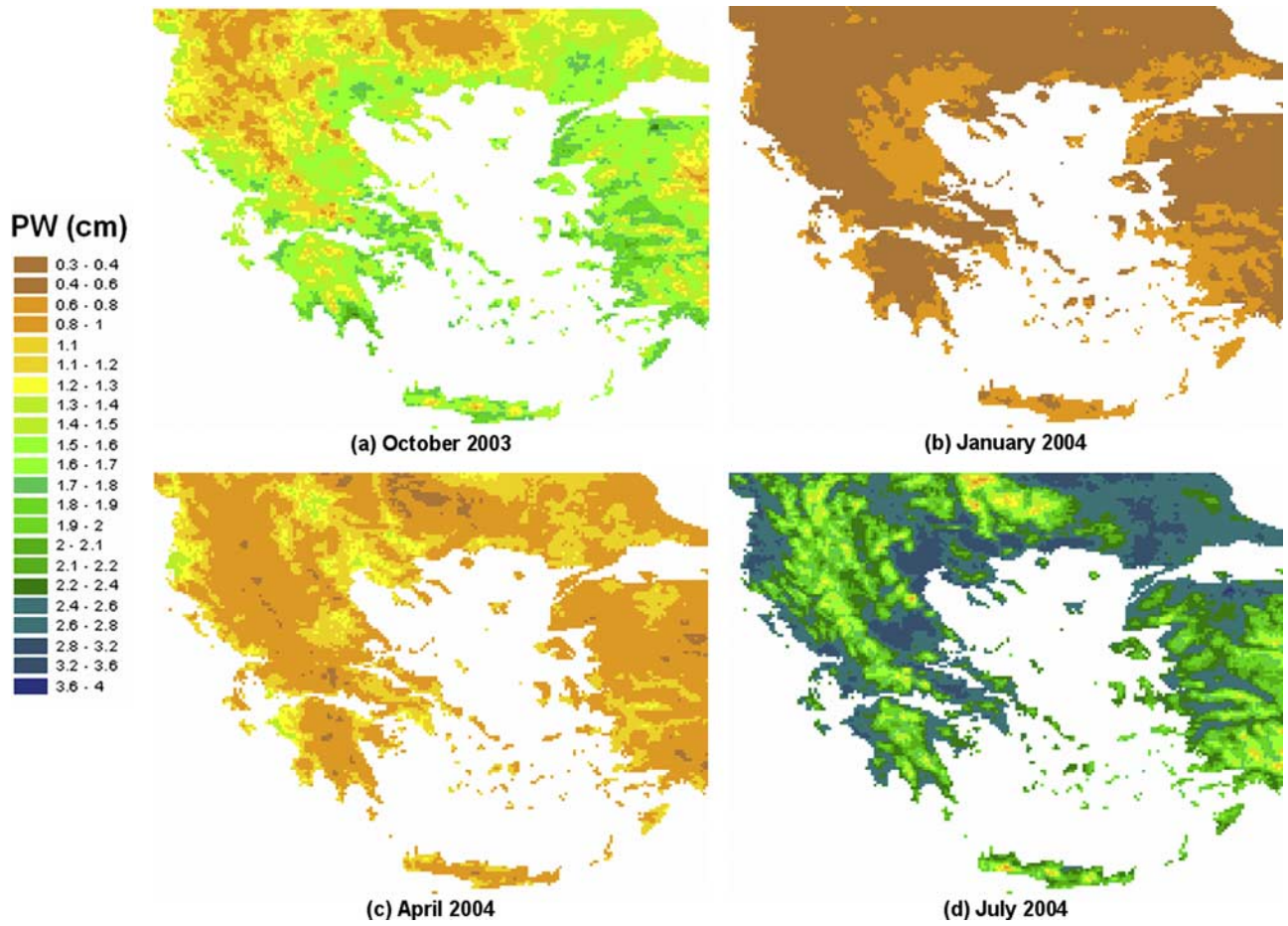

Figure 5. Monthly mean values of PW (cm) over the study area in a 5 × 5 km cell grid. Monthly means were calculated on the basis of MODIS Level 2 precipitable water product, therefore they are representative for the morning case (around the time of Terra pass over the study area): (a) October 2003; (b) January 2004; (c) April 2004 and (d) July 2004. The maximum values of the spatial distribution of the mean PW are 2.33, 0.98, 1.48 and 3.86 cm, respectively.

were pre-processed and outliers, which resulted either due to missing temperature or humidity values at specific heights or due to interpolation or extrapolation errors, were removed.

[43] Next, to estimate the spatial distribution of the approximate $\frac{\partial PW(x,y,t_0)}{\partial t}$ term, an inverse (squared) distance weighting scheme over the study area was employed, based on PW values obtained at the four synoptic stations. The output grid cell size was again set equal to 5 × 5 km. Application of a spatial interpolation method to data from four sites may seem a crude approximation of the spatial dynamics of the rate of change of PW. However, our data suggested that these rates did not display large spatial variability, therefore the approximation error was expected to be small. It should be noted that given the low spatial resolution the radiosonde data, this simple interpolation scheme seems the most adequate for this study.

[44] As a result a $\frac{\partial PW(x,y,t_0)}{\partial t}$ value was calculated in each cell, corresponding to a PW(x, y, t) value. Finally the parameter PW*(x, y, t_0) was calculated for each grid cell. The spatial distribution of PW* over the study area and the respective spatial distribution of AVHRR derived ΔT were afterward used to estimate the coefficients a and b in equation (4) by means of robust regression analysis.

3.6. Robust Regression Analysis

[45] The unknown parameters in equation (4) were estimated via a robust regression procedure. The main purpose of robust regression is to detect outliers and provide resistant (stable) estimates for the coefficients of a linear relationship. Historically, three classes of problems have been addressed with robust regression techniques: Problems with outliers in the y-direction (which in our case means extreme values for PW*); problems with outliers in the x-space, also referred to as leverage points (which in our case means extreme values for ΔT) and problems with outliers in both directions. As explained in section 4, in this work, all the abovementioned cases were encountered.

[46] Outliers were identified via Least Trimmed Squares (LTS) estimation of the regression coefficients. LTS is a high breakdown value method introduced by *Rousseeuw* [1984]. Roughly speaking, the breakdown value is a measure for the proportion of contamination that an estimation method can withstand and still maintain its robustness. LTS regression is based on a subset of observations whose least

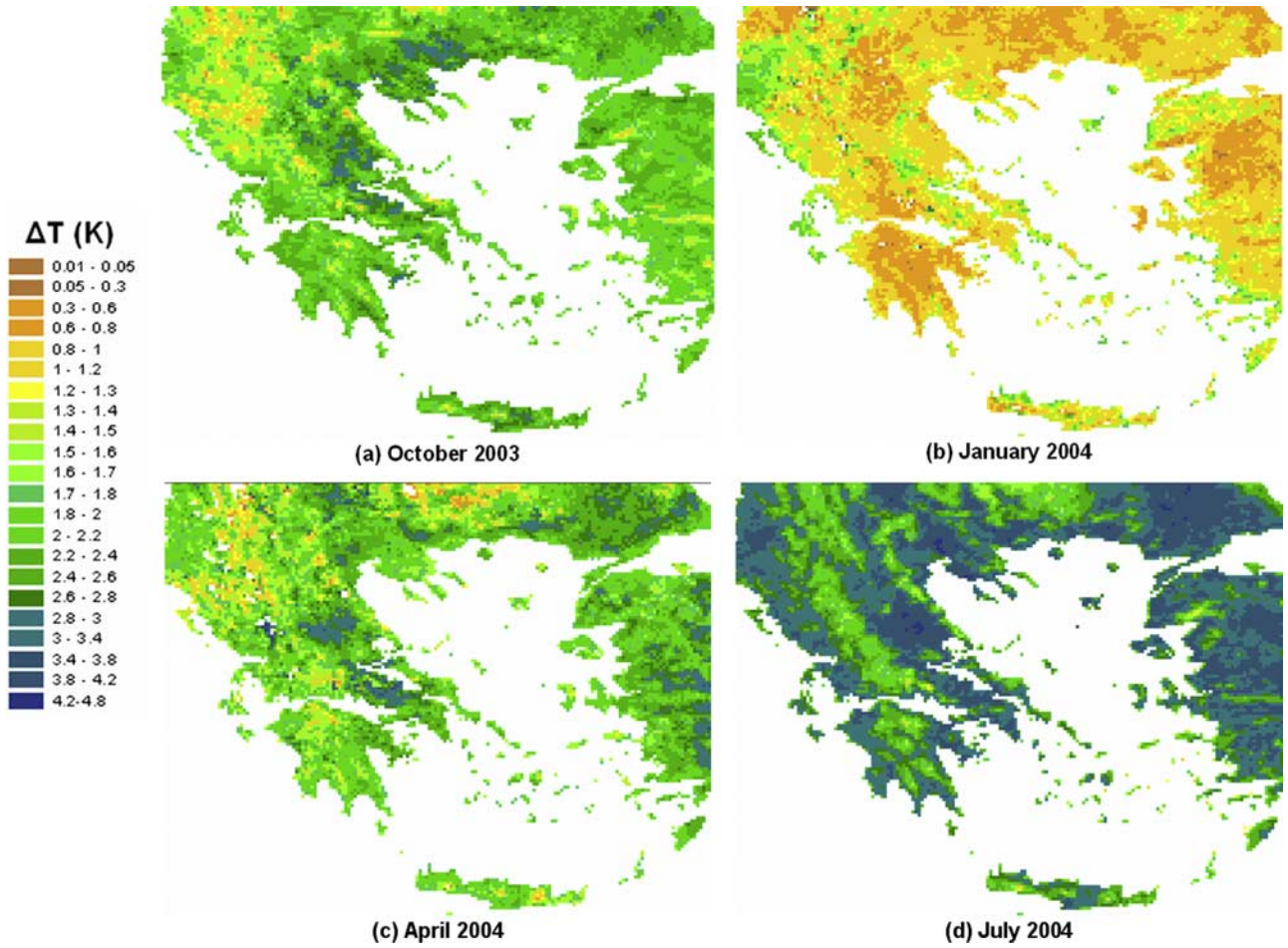

Figure 6. Monthly mean values of ΔT (K) over the study area in a 5×5 km cell grid. Monthly means were calculated on the basis of NOAA 16 AVHRR thermal infrared records, therefore they are representative for the morning–mid day case (around the time of NOAA16 pass over the study area): (a) October 2003; (b) January 2004; (c) April 2004 and (d) July 2004. The maximum values of the spatial distribution of the mean ΔT are 3.62, 3.97, 4.78 and 4.59 K, respectively.

squares fit possesses the smallest sum of squared residuals. The performance of this method was improved by the FAST-LTS algorithm of *Rousseeuw and Van Driessen* [2000]; since our model contains a single regressor we applied the exact algorithm of *Rousseeuw and Leroy* [1987].

[47] Outlier diagnostics were based on the residuals of the LTS regression. In particular, leverage points were identified using the Mahalanobis and robust minimum covariance determinant (MCD) distances, and outliers were identified from the values of standardized robust residuals. A pair of PW*-ΔT values was characterized as a leverage point, or an outlier, if the corresponding distances exceed some predefined cutoff values (see *Hubert et al.* [2005], for further details). The last stage of the robust regression procedure computed the final weighted least squares estimates, which were least squares estimates computed after deleting the detected outliers.

3.7. Application and Validation

[48] The PW*-ΔT relationship was applied to produce PW spatial distributions over the study area using AVHRR thermal infrared measurements. As previously noted, ΔT was estimated for cloud free pixels of geometrically corrected scenes acquired over the study area for the period 2001 to 2005. Daytime acquisitions of NOAA 16 for each day of the mid month of each season (January, April, July, and October) were used. Hence the spatiotemporal distribution of PW on the basis of equation (4) was produced. Moreover, to examine interannual and spatial variability, seasonal means for the study period (2001–2005) were calculated using the time series of the spatial distribution of PW for January, April, July and October.

[49] To validate our PW estimates, radiosonde derived PW values at Athens, Thessaloniki, Heraklion and Izmir synoptic stations were used. It was assumed that the radiosonde measurements at each synoptic station were representative for the 5×5 km cell in which the station was included. Therefore the radiosonde derived PW corresponding to the station location, was assigned to the respective grid cell. In this way, the radiosonde derived PW and the AVHRR derived PW can be compared at cell level.

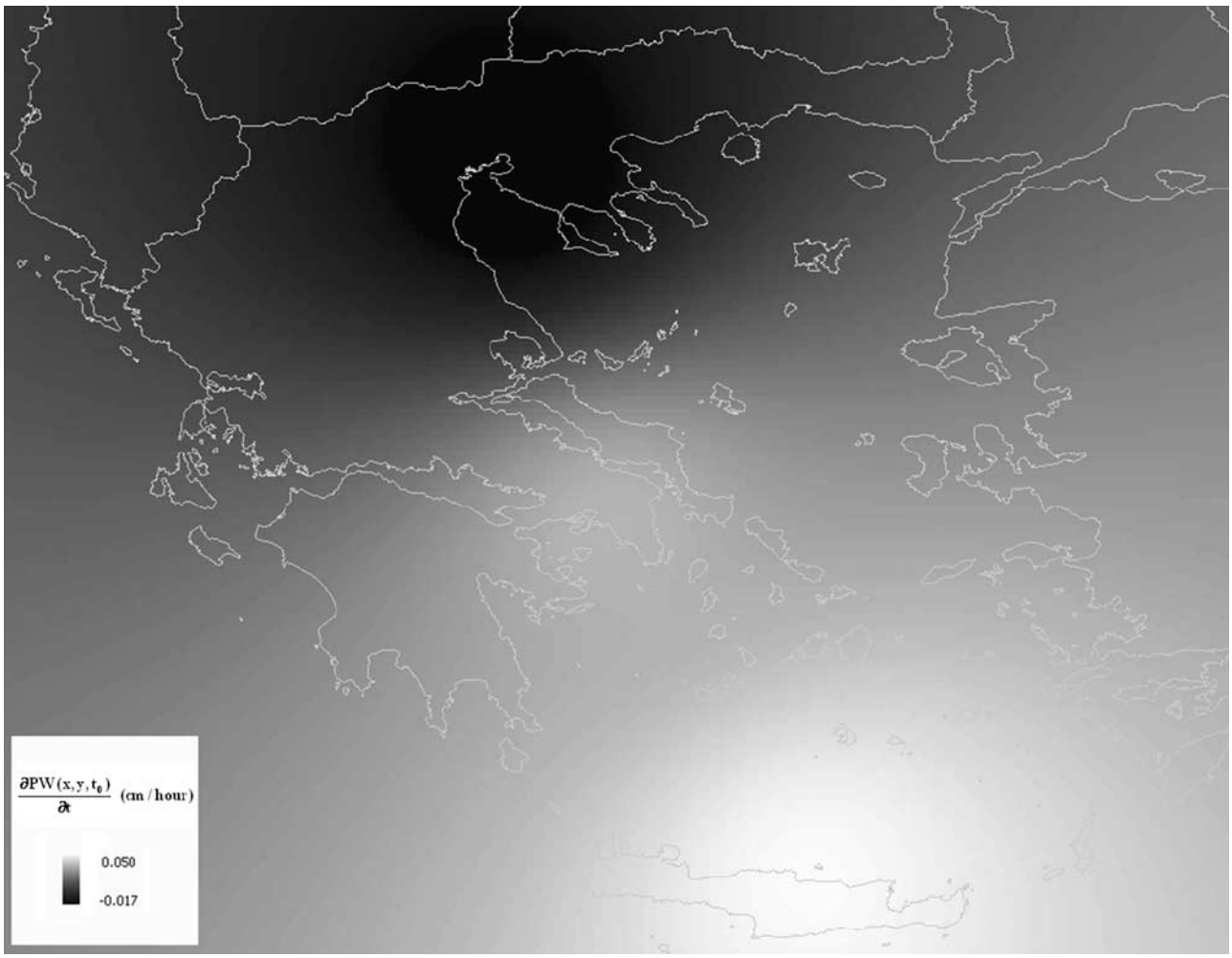

Figure 7. $\frac{\partial PW(x,y,t_0)}{\partial t}$ spatial distribution for October 12, 2003 at 12:45 UTC, as derived by spatial interpolation using the $\frac{\partial PW(t_0)}{\partial t}$ values at Athens, Thessaloniki, Heraklion and Izmir stations, which were estimated from radiosonde data.

[50] To measure how close PW estimates were to the observed radiosonde values, the Root Mean Square Error (RMSE) was calculated for the cloud free cells corresponded to the locations of the above synoptic stations. Validation was performed for days with no missing radiosonde measurements (at 12:00 UTC) for each of the months January (153 pairs), April (185 pairs), July (272 pairs) and October (221 pairs) of the time period 2001–2005, as well as for the whole data set (831 pairs). Moreover, to visualize biases in estimation, scatterplot diagrams of the estimated versus the observed values were used.

4. Results and Discussion

[51] Monthly means of radiosonde-derived PW measurements for 00:00 UTC and 12:00 UTC at Athens, Thessaloniki, Heraklion and Izmir synoptic stations, clearly reveal the interannual variability of atmospheric humidity as shown in Figure 3. This phenomenon is also displayed in Figure 4, which presents an example of daily PW time series as calculated using the 12:00 UTC radiosonde measurements of Athens synoptic station for the period 2001–2005. A moving average has been superimposed (bold curve), which makes the summer maxima and the winter minima of PW evident.

[52] The analysis of MODIS Level 2 PW product was performed for October 2003, January, April and July of 2004. The spatial distribution of PW, as derived by daily MODIS observations over the study area, was estimated at 5 × 5 km cell level. Figure 5 displays the spatial distribution of MODIS-derived PW at 5 × 5 km level; mean values for the mid month of each season are presented. PW values over land were used, given that in this case the MODIS near infrared PW retrievals were reliable. The effect of topography is evident: lower PW values are observed over the west part of central and northern Greece (Pindos mountain chain), over the mountainous area of central Peloponnese, over the three main mountain chains of the Crete island, as well as over the mountainous areas of Turkey, Albania, Bulgaria and Former Yugoslavian Republic of Macedonia, for all seasons. Moreover the summer maxima and the winter minima of the PW distribution are depicted: mean PW maxima of 2.33, 0.98, 1.48 and 3.86 cm, correspond to October, January, April and July, respectively.

Table 3. Final Weighted Least Squares Estimates for the Coefficients of Equation (4)[a]

FWLS	Coeff.	S.E.	Chi-square	P-value
Const.	0.362 (0.309)	0.005	4418	<0.0001
ΔT	0.719 (0.742)	0.002	8913	<0.0001
		R^2: 0.823		
LS	Coeff.	S.E.	t-value	P-value
Const.	0.371 (0.369)	0.006	65.07	<0.0001
ΔT	0.716 (0.717)	0.003	285.03	<0.0001
		R^2: 0.731		

[a]The coefficients are estimated after the removal of outliers and leverage points which are identified after fitting a least trimmed squares robust regression on the PW*-ΔT pairs. OLS estimates are presented as well. Chi-square and t statistics together with the corresponding p-values indicate that all estimates are statistically significant. Note: LTS estimates are presented in parentheses under the corresponding FWLS estimates; LS estimates after the removal of the 4 outliers identified from LS residuals are presented in parentheses under the corresponding LS estimates.

[53] Figure 6 displays the spatial distribution of AVHRR-derived ΔT for the same months. ΔT maxima for October, January, April, and July, are recorded as 3.62, 3.97, 4.78 and 4.59 K, respectively. A correspondence of monthly mean PW and ΔT spatial patterns is observed for all cases of Figures 4 and 5.

[54] The absolute maximum $\frac{\partial PW(x,y,t_0)}{\partial t}$ values over the study area found to range from 0.035 to 0.330 cm/hour for the 15 days of Table 1. Figure 7 shows the spatial distribution of the estimated $\frac{\partial PW(x,y,t_0)}{\partial t}$ term, for October 12, 2003 at 12:45 UTC as an example. One may observe the effect of the inverse (squared) distance-weighting scheme in estimated rates. Maximum PW rates of change of 0.05 cm/hour are observed for this case.

[55] A standard OLS analysis for the estimation of the unknown coefficients in equation (4), revealed the presence of only 4 outliers, among the 29861 PW*-ΔT pairs contained in the data set of this study. However, a robust LTS analysis revealed that 0.77% of the PW*-ΔT pairs classified as outliers according to their robust standardized residuals and 0.14% of the pairs classified as leverage points according to their Mahalanobis and Robust MCD distances. Table 3 indicates a substantial improvement in the fit of the final weighted least squares estimates, that is the estimates that emerged after LTS identified residuals were removed from the data set. Indeed, the corresponding values for the goodness of fit statistics were $R^2_{FWLS} = 0.823$ and $R^2_{LS} = 0.731$ for the FWLS and LS regression, respectively. Outlying values had also some impact on the magnitude of the estimates. This impact was not dramatic though, given the proportion and magnitude of outliers. A scatterplot of the PW*-ΔT pairs together with the FWLS and LTS regression lines is presented in Figure 8.

[56] The spatial distribution of the AVHRR derived mean PW for the months January, April, July and October of the

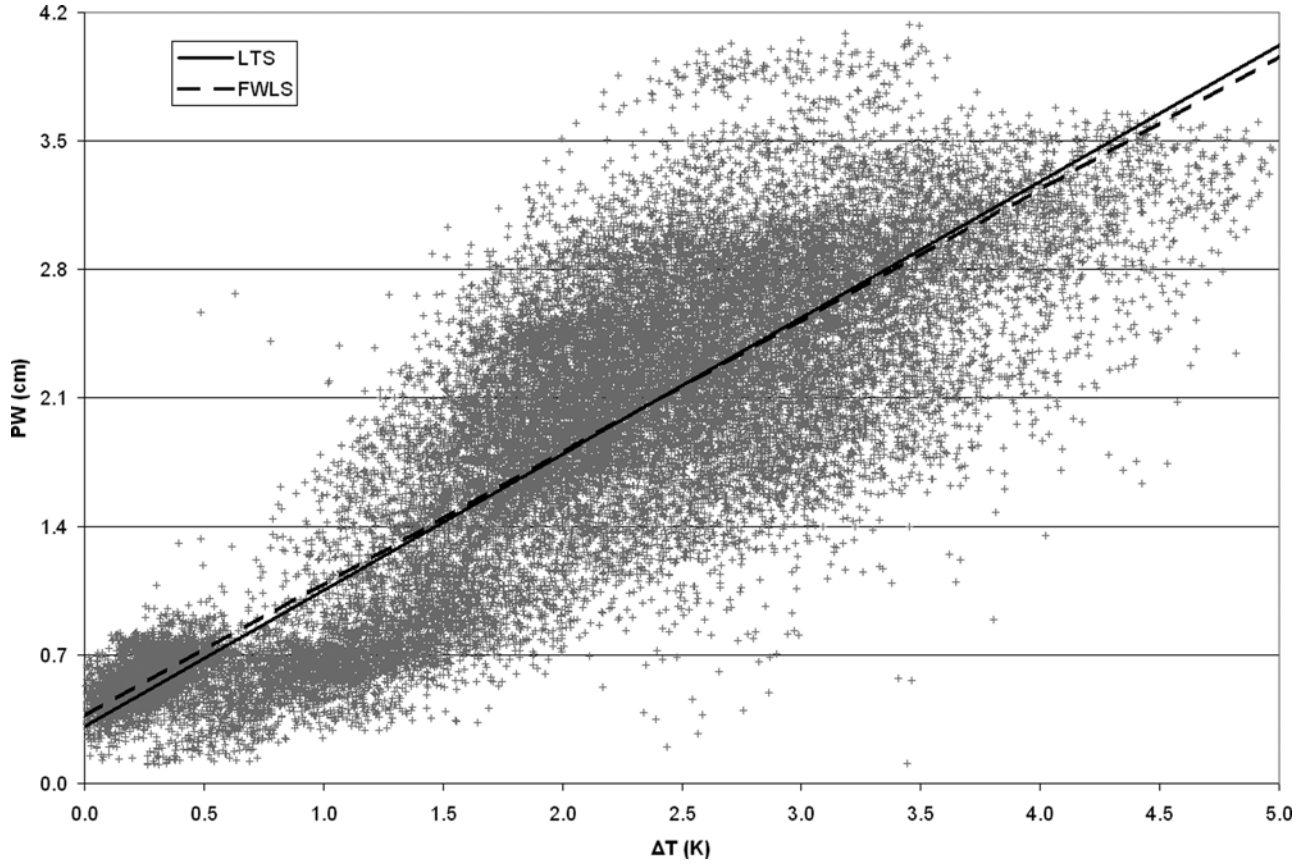

Figure 8. A scatterplot of PW* versus ΔT that depicts the Robust Least Trimmed Squares and the Final Weighted Least Squares Regression lines.

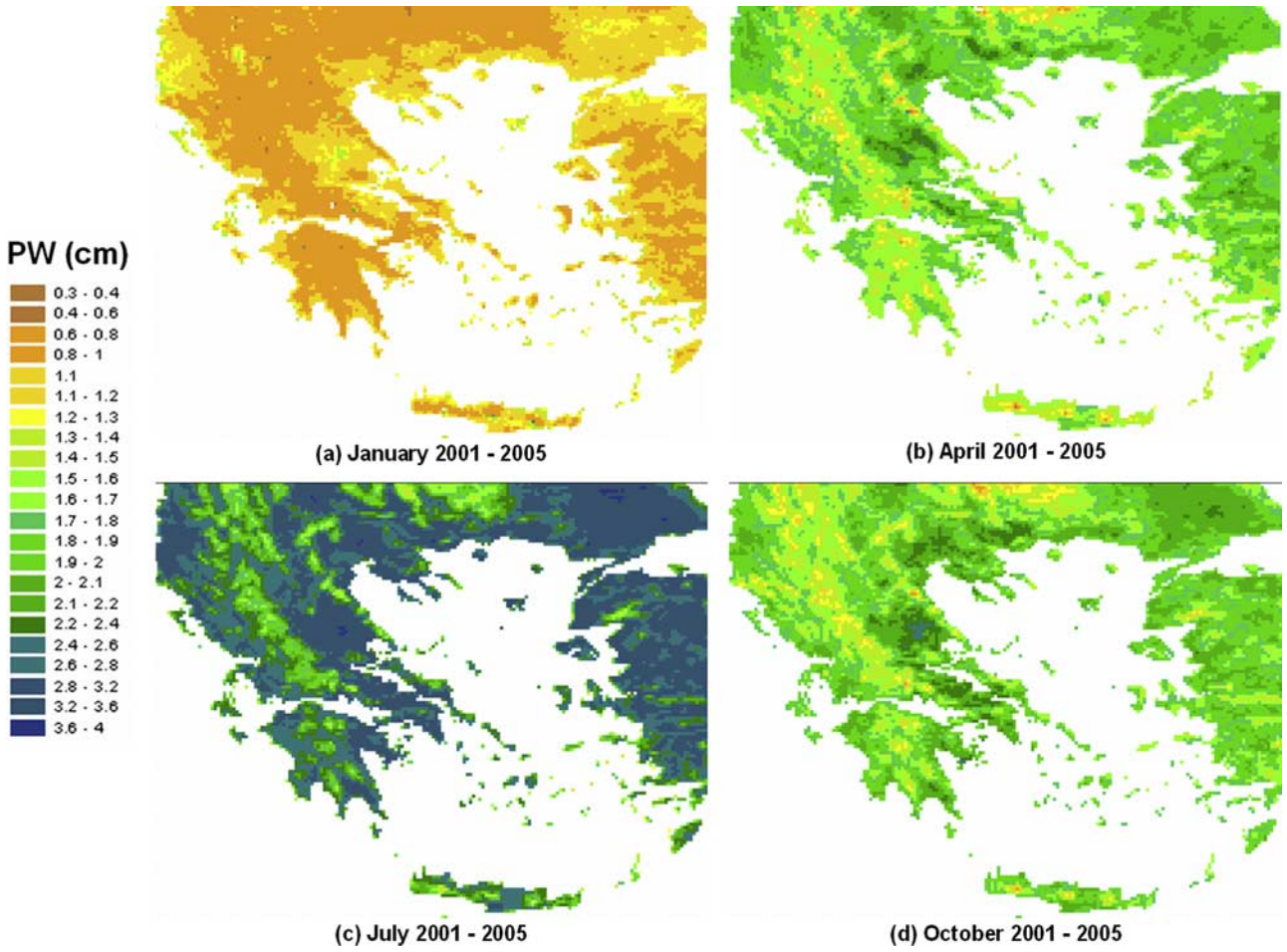

Figure 9. The spatial distribution of AVHRR derived PW values estimated at each grid cell by averaging the daily values for the whole 2001–2005 period for January (a), April (b), July (c) and October (d). The seasonal, as well the spatial variability of PW is indicated.

period 2001–2005 is shown in Figure 9, where the PW interannual and spatial variability can be observed. The summer maxima and the winter minima are evident in each cell and the effect of topography is shown as well. Mean PW maxima of 1.60, 2.61, 3.96, and 2.50 cm are observed for January, April, July, and October, respectively.

[57] However, of particular importance are the local maxima, which can be observed over Thessaly, Central Macedonia, East Thrace, West Albania and several less extended parts of the West Greece and Turkey, especially in the summer. All these areas are almost flat areas with high percentage of arable land. Irrigated cultivation patterns can be found in most of these areas. Irrigation favors evapotranspiration, it therefore contributes to the increase of the atmospheric humidity amounts during the growing season, as well as during the summer. Finally, it is well known that atmospheric humidity (and thus PW) increases with air temperature. The spatial patterns of air temperature over the study area are highly affected by the topography and are consistent with the observed PW patterns, especially during the summer [*Xoplaki et al.*, 2003].

[58] The spatial distribution of the monthly mean PW difference (ΔPW) between July and January of the period 2001–2005 is shown in Figure 10. It is an indicator of the spatial distribution of humidity difference between the warm and the cold period in the study area. The topography effect is also evident in Figure 10, since lower differences are observed over mountainous areas. Of particular importance is the low relative ΔPW values which are observed over eastern Crete. This may be explained by the action of the Etesians (North winds blowing over the Aegean Sea during the summer, especially in July). If the Etesians were not blowing over this area during the summer, the air temperature would be higher and therefore the monthly mean PW value for July would be higher. Consequently, the ΔPW would be also higher.

[59] Figure 11 shows scatter diagrams of radiosonde derived PW versus AVHRR derived PW for January (a), April (b), July (c), and October (d) for the whole study period, 2001–2005. The respective RMSE were estimated at 0.46, 0.39, 0.52, and 0.45 cm. Visual inspection of these scatterplots and estimation of linear regressions via OLS indicated the presence of some bias in AVHRR derived PW

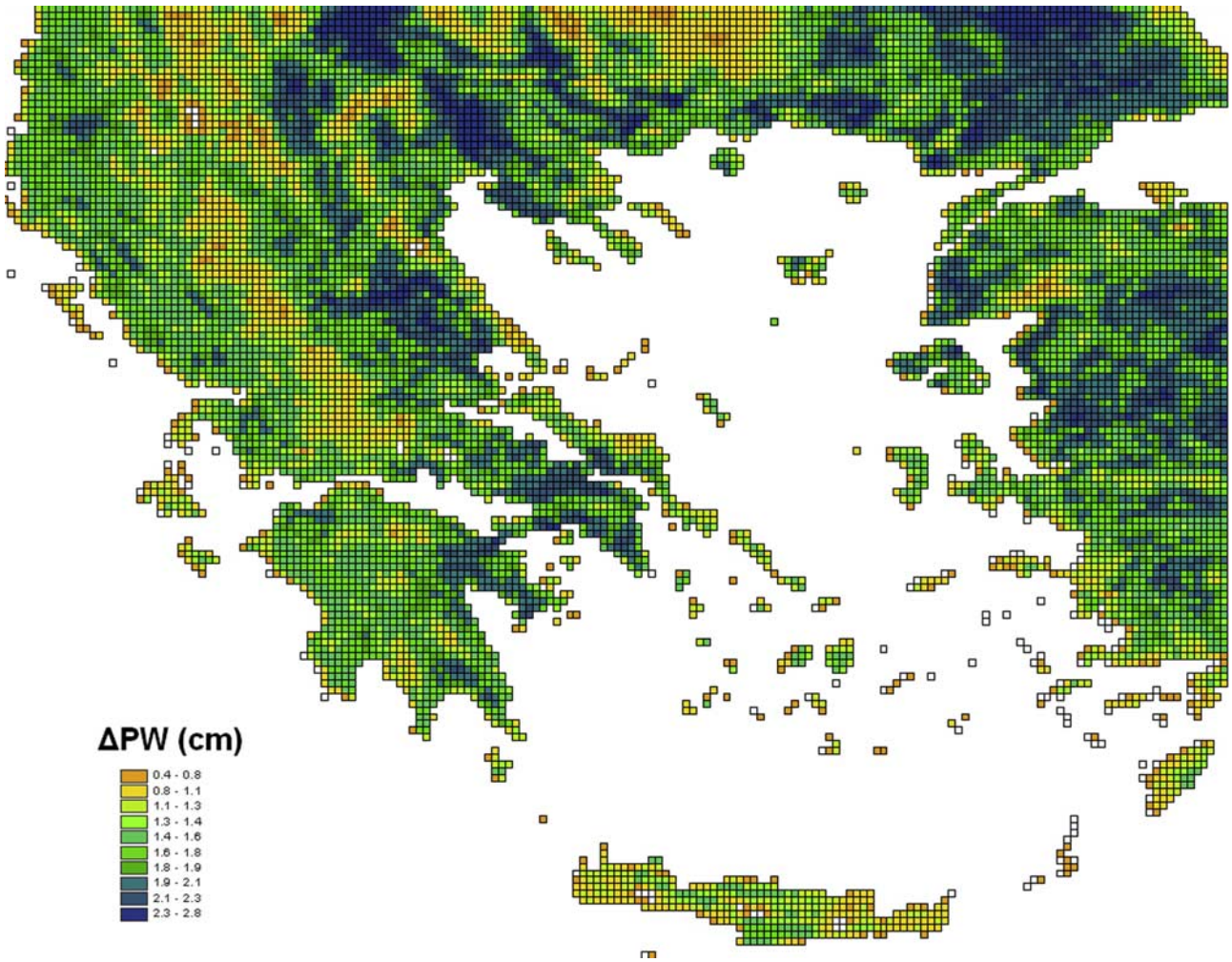

Figure 10. Monthly mean PW differences between the warm and the cold periods calculated by subtracting the monthly mean value of January from the respective value of July for each grid cell for the whole period 2001–2005.

estimates. This finding indicates that the linear model in (4) could be refined by allowing for seasonal effects. We plan to explore this issue in further research.

[60] Figure 12 depicts a scatter diagram of radiosonde derived PW versus AVHRR derived PW for the whole period 2001–2005 (four months). Radiosonde derived PW values were found to be highly correlated with their corresponding AVHRR estimates; indeed, Pearson's correlation coefficient was found equal to 0.812. Standard OLS estimation revealed that the intercept of the regression line equals $b_{OLS} = 0.25$ and the corresponding slope equals $a_{OLS} = 0.87$. Hence the best fitting line is close to the line with zero intercept and unit slope displayed in Figure 12, indicating the overall absence of bias in AVHRR estimation. The respective RMSE was estimated at 0.46 cm, which indicated a very good agreement of estimated and observed parameters.

[61] Finally, separate OLS regressions between radiosonde derived PW and AVHRR derived PW were also carried out for each year of the study period (results are not shown for space economy). The corresponding estimates for each year are very close to the values reported above for the equation that concerns the full validation data set. This finding supports the temporal stability of our predictions that were based on the robust regression model.

5. Conclusions

[62] The knowledge of the spatiotemporal distribution of PW is important for hydrological, climatological and meteorological applications, in evapotranspiration studies and in biospheric and atmospheric modeling. PW is also needed to atmospherically correct optical imagery, as well as to correct SAR interferometric measurements. In this study the spatial distribution of PW was extracted from AVHRR thermal channels brightness temperature difference. The relationship between PW and ΔT was calibrated by robust regression using the MODIS derived PW and validated using radiosonde measurements. Radiosonde derived PW rates of change were also used to adjust the MODIS derived PW to the AVHRR acquisition time. The application area was the broader area of Greece and all spatial calculations were performed in a 5×5 km cell grid.

[63] The PW–ΔT relationship was calibrated using cloud free cells from 15 days distributed in October 2003, January, April, and July 2004. The two variables were highly

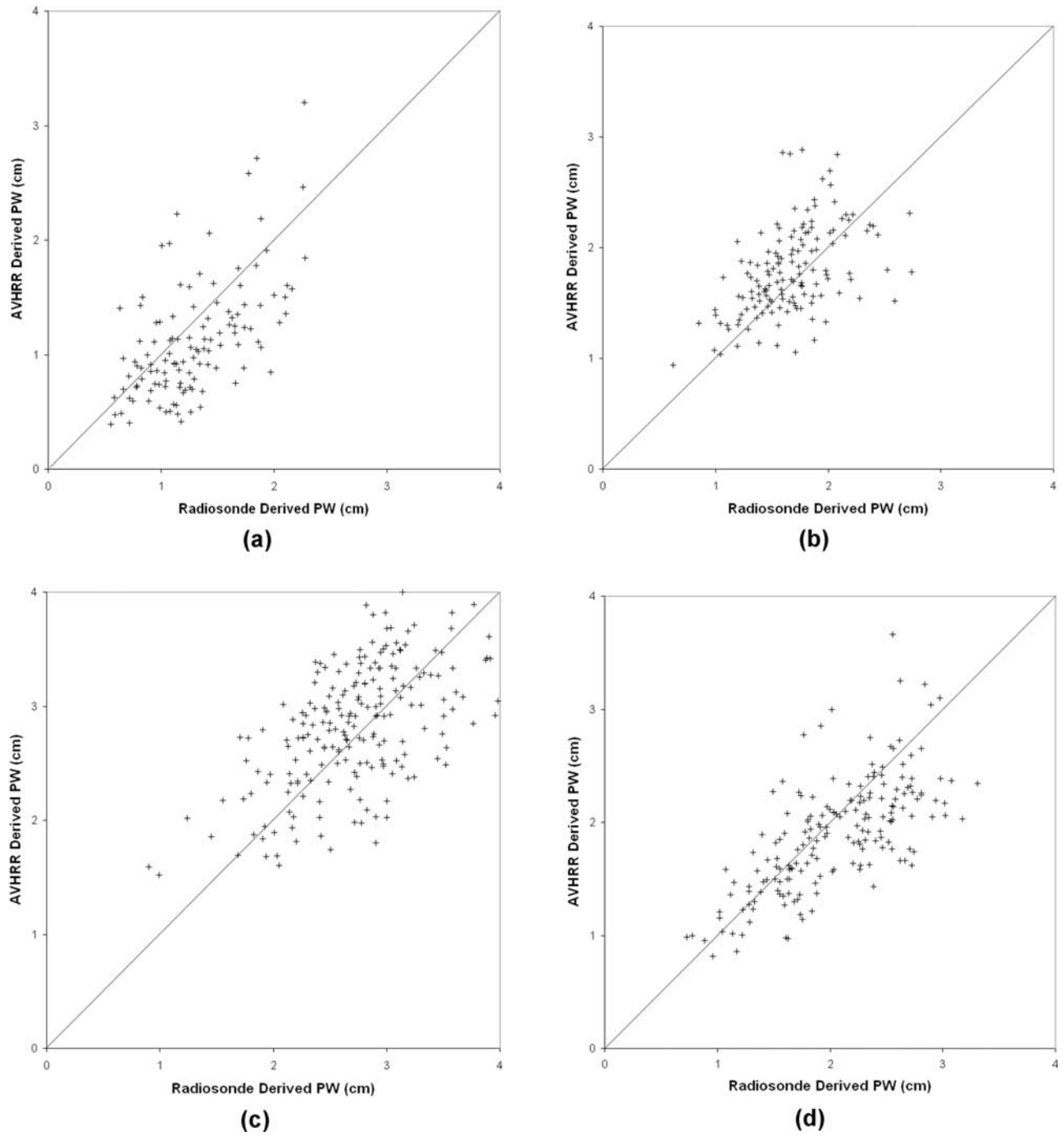

Figure 11. Scatter diagrams of AVHRR derived PW (estimated) versus radiosonde derived PW (observed) values for January (a), April (b), July (c) and October (d) of the period 2001–2005.

correlated and although the regression sample was high (29861 pairs) the resulted equation was estimated with a correlation coefficient of 91% by employing robust regression analysis methods. This equation was applied to daily ΔT data for January, April, July and October of the five years period 2001–2005. The PW spatial-temporal distribution was derived in this way from AVHRR records and its spatial and interannual variability was assessed. The resulted PW values were validated using radiosonde measurements and a very good agreement between radiosonde and AVHRR derived PW values was observed (RMSE = 0.46 cm).

[64] A correspondence of the spatial patterns of MODIS derived PW and AVHRR derived ΔT was observed. The effect of topography was evident since lower PW and ΔT values were observed for all seasons, over the west part of central and northern Greece (Pindos mountain chain), over the mountainous area of central Peloponnese, over the three main mountain chains of the Crete island, as well as over the mountainous areas of Turkey, Albania, Bulgaria and

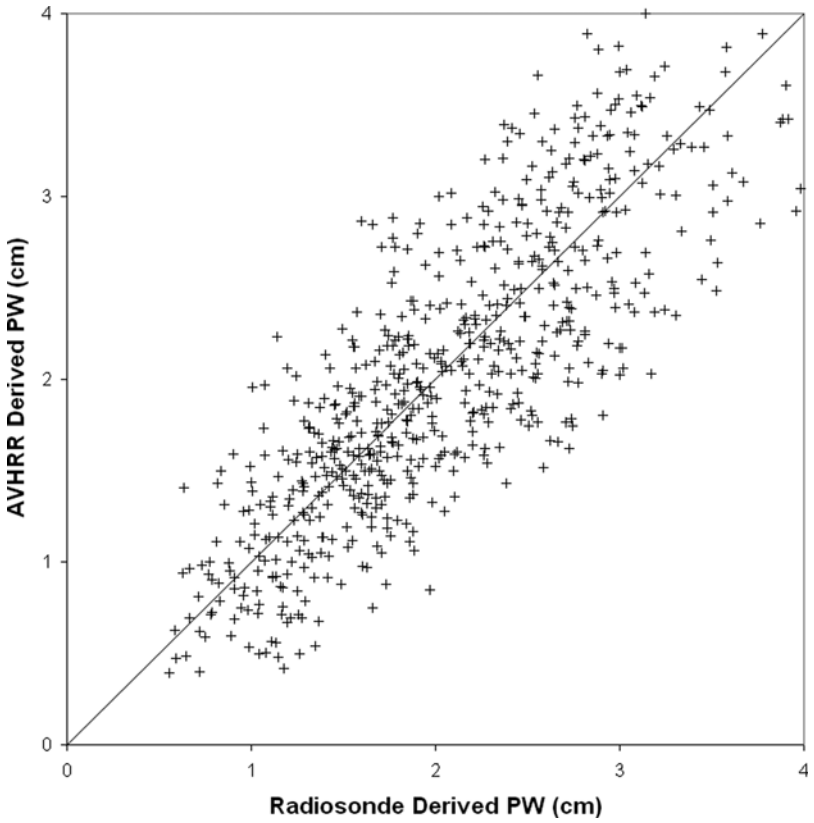

Figure 12. Scatter diagrams of AVHRR derived PW (estimated) versus radiosonde derived PW (observed) values for the whole period 2001–2005.

Former Yugoslavian Republic of Macedonia. The PW interannual and spatial variability were observed from the AVHRR derived PW spatial distributions of the period 2001–2005. The summer maxima, the winter minima and the effect of topography were evident in each cell. Mean PW maxima of 1.60, 2.61, 3.96, and 2.50 cm for the study area were observed for January, April, July and October, respectively. Moreover local scale maxima were observed over Thessaly, Central Macedonia, East Thrace, West Albania and several less extended parts of the West Greece and west Turkey, especially in the summer.

[65] The main achievements of the present study are:

[66] ● a methodology to combine MODIS and AVHRR records for PW estimation;

[67] ● a site specific PW-ΔT relationship which can be used to provide consistent estimates of PW for a multiyear database, by analyzing time series of accurately calibrated AVHRR channels 4 and 5 radiances;

[68] ● a five year spatial distribution of PW on a daily basis (for January, April, July, and October) at 5 $\times$ 5 km cells over the study area, which can be used in several applications sensitive to PW spatial variability as discussed above;

[69] ● the use of robust regression analysis techniques to estimate the PW-ΔT relationship;

[70] ● the use of an extended validation data set.

[71] Future work may focus on the synergy of AVHRR, MODIS and other sensors, such as the Spinning Enhanced Visible and InfraRed Imager (SEVIRI) onboard MSG, to assess the diurnal variability of PW and its modifications in space and time. It may also focus on the improvement of the AVHRR derived PW accuracy by taking also into account the effect of the atmospheric path on the attenuation of thermal infrared radiation, which is a function of the satellite zenith angle. The accuracy of the AVHRR derived PW could be also improved by taking into account the geophysical parameters that mainly affect the PW, namely the topography, the surface temperature and emissivity.

[72] **Acknowledgments.** This work was conducted in the framework of the PRECIPITABLE WATER (Study on the spatial–temporal distribution of atmospheric water content with the combined use of satellite remote sensing and non-linear science) project funded by the Program "Competitiveness", Measure 4.3, Action 4.3.6.1 of the General Secretary of Research and Technology of the Ministry of Development of Greece and the Ministry of Science and Technology of Peoples' Republic of China.

References

Alishouse, J. C., S. A. Snyder, J. Vongsathorn, and R. R. Ferraro (1990), Determination of oceanic total precipitable water from the SSM/I. IEEE, *IEEE Trans. Geosci. Remote Sens.*, *28*, 811–816.

Andersen, H. S. (1996), Estimation of precipitable water vapour from NOAA-AVHRR during the Hapex Sahel experiment, *Int. J. Remote Sens.*, *17*, 2783–2801.

Barton, J., and A. J. Prata (1999), Difficulties associated with the application of covariance–variance techniques to retrieval of atmospheric water vapor from satellite imagery, *Remote Sens. Environ.*, *69*, 76–83.

Bony, S., and J. P. Duvel (1994), Influence of the vertical structure of the atmosphere on the seasonal variation of precipitable water and greenhouse effect, *J. Geophys. Res.*, *99*, 12,963–12,980.

Bouffies, S., F. M. Breon, D. Tanre, and P. Dubuisson (1997), Atmospheric water vapor estimate by a differential absorption technique with the polarization and directionality of the Earth reflectances (POLDER) instrument, *J. Geophys. Res.*, *102*, 3831–3841.

Cartalis, C., and N. Chrysoulakis (1997), Estimation of precipitable water in Greece on the basis of radiosondes and satellite data, *Toxicol. Environ. Chem.*, *58*, 163–171.

Chesters, D., L. W. Uccellini, and W. D. Robinson (1983), Low level water vapour fields from the VISSR Atmospheric Sounder (VAS) "splitwindow" channels, *J. Clim. Appl. Meteorol.*, *22*, 725–743.

Choudhury, B. J., and N. E. Di Girolamo (1995), Quantifying the effect of emissivity on the relations between AVHRR split window temperature difference and atmospheric precipitable water over land surfaces, *Remote Sens. Environ*, *54*, 313–323.

Choudhury, B. J., T. J. Dorman, and A. Y. Hsu (1995), Modeled and observed relations between the AVHRR split window temperature difference and atmospheric precipitable water over land surfaces, *Remote Sens. Environ.*, *51*, 281–290.

Chrysoulakis, N., and C. Cartalis (2000), Distribution of precipitable water in Southern Greece in support of solar radiation models, *Int. J. Sol. Energy*, *20*, 197–206.

Chrysoulakis, N., and C. Cartalis (2002), Improving the estimation of land surface temperature for the region of Greece: Adjustment of a split window algorithm to account for the distribution of precipitable water, *Int. J. Remote Sens.*, *23*, 871–880.

Chrysoulakis, N., and C. Cartalis (2003), A new algorithm for the detection of plumes caused by industrial accidents, on the basis of NOAA/AVHRR imagery, *Int. J. Remote Sens.*, *24*, 3353–3367.

Chrysoulakis, Í., M. Proedrou, and C. Cartalis (2001), Variations and trends in annual and seasonal means of precipitable water in Greece as deduced from radiosonde measurements, *Toxicol. Environ. Chem.*, *84*, 1–6.

Czajkowski, K. P., S. N. Goward, D. Shirey, and A. Walz (2002), Thermal remote sensing of near-surface water vapor, *Remote Sens. Environ.*, *79*, 253–263.

Dalu, G. (1986), Satellite remote sensing of atmospheric water vapour, *Int. J. Remote Sens.*, *7*, 1089–1097.

Eck, T. F., and B. N. Holben (1994), AVHRR split window temperature differences and total precipitable water over land surfaces, *Int. J. Remote Sens.*, *15*, 567–582.

Elliott, W. P., and D. J. Gaffen (1991), On the utility of radiosonde humidity archives for climate studies, *Bull. Am. Meteorol. Soc.*, *72*, 1507–1520.

Frouin, R., P. Y. Deschamps, and P. Lecomte (1990), Determination from space of atmospheric total water vapor amounts by differential absorption near 940 nm: Theory and airborne verification, *J. Appl. Meteorol.*, *29*, 448–460.

Gaffen, D. J., A. Robock, and W. P. Elliott (1992), Annual cycles of tropospheric water vapor, *J. Geophys. Res.*, *97*, 18,185–18,193.

Gao, B.-C., and A. F. H. Goetz (1990), Column atmospheric water vapor and vegetation liquid water retrievals from airborne imaging spectrometer data, *J. Geophys. Res.*, *95*, 3549–3564.

Gao, B.-C., and Y. J. Kaufman (2003), Water vapor retrievals using Moderate Resolution Imaging Spectroradiometer (MODIS) near-infrared channels, *J. Geophys. Res.*, *108*(D13), 4389, doi:10.1029/2002JD003023.

Goodrum, G., B. K. Kidwell, and W. Winston (Eds) (2001), *NOAA KLM USER'S GUIDE*, U. S. Department of Commerce, National Oceanic and Atmospheric Administration National Environmental Satellite, Data, and Information Service, National Climatic Data Center, Climate Services Division, Satellite Services Branch, FOB3, Room G227, E/CC33, 5200 Auth Road, Suitland, MD 20746-4304, USA.

Goward, S. N., R. H. Waring, D. G. Dye, and J. Yang (1994), Ecological remote sensing at OTTER: Macroscale satellite observations, *Ecol. Appl.*, *4*, 322–343.

Guillory, A. R., G. J. Jedlovec, and H. E. Fuelberg (1993), A technique for deriving column-integrated water content using VAS split-window data, *J. Appl. Meteorol.*, *32*, 1226–1241.

Harris, A. R., and I. M. Mason (1992), An extension to the split-window technique giving improved atmospheric correction and total water vapour, *Int. J. Remote. Sens.*, *5*, 881–892.

Halthore, R. N., T. F. Eck, B. N. Holben, and B. L. Markham (1997), Sun photometric measurements of atmospheric water vapor column abundance in the 940-nm band, *J. Geophys. Res.*, *102*, 4343–4352.

Hanssen, R. F., A. J. Feijt, and R. Klees (2001), Comparison of precipitable water vapor observations by spaceborne radar interferometry and Meteosat 6.7-μm radiometry, *J. Atmos. Oceanic Technol.*, *18*, 756–764.

Hubert, M., P. J. Rousseeuw, and S. VanAelst (2005), Multivariate outlier detection and robustness, *Hand. Stat.*, *24*, 263–302.

Iribarne, J. V., and W. L. Godson (1981) *Atmospheric Thermodynamics* (Second Edition), Geophysics and Astrophysics Monographs, D. Reidel Publishing Company, Dordrecht, Holland.

Jade, S., M. S. M. Vijayan, V. K. Gaur, T. P. Prabhu, and S. C. Sahu (2005), Estimates of precipitable water vapour from GPS data over the Indian subcontinent, *J. Atmos. Sol. Terr. Phy.*, *67*, 623–635.

Jedlovec, G. J. (1990), Precipitable water estimation from high-resolution split window radiance measurement, *J. Appl. Meteorol.*, *29*, 863–877.

Jiménez-Muñoz, J. C., and J. A. Sobrino (2005), Atmospheric water vapour content retrieval from visible and thermal data in the framework of the DAISEX campaigns, *Int. J. Remote Sens.*, *26*, 3163–3180.

Johnsen, K.-P., and S. Q. Kidder (2002), Water vapor over Europe obtained from remote sensors and compared with a hydrostatic NWP model, *Phys. Chem. Earth*, *27*, 371–375.

Justice, C. O., T. F. Eck, D. Tanre, and B. N. Holben (1991), The effect of water vapour on the normalized difference vegetation index derived for the Sahelian region from NOAA AVHRR data, *Int. J. Remote Sens.*, *12*, 1165–1187.

Kaufman, Y. J., and B.-C. Gao (1992), Remote sensing of water vapor in the near IR from EOS/MODIS, *IEEE Trans. Geosci. Remote Sens.*, *30*, 871–884.

King, M. D., Y. J. Kaufman, W. P. Menzel, and D. Tanre (1992), Remote sensing of cloud, aerosol and water vapor properties from the Moderate Resolution Imaging Spectrometer (MODIS), *IEEE Trans. Geosci. Remote Sens.*, *30*, 1–27.

King, M. D., W. P. Menzel, Y. J. Kaufman, D. Tanré, B.-C. Gao, S. Platnick, S. A. Ackerman, L. A. Remer, R. Pincus, and P. A. Hubanks (2003), Cloud and aerosol properties, precipitable water, and profiles of temperature and water vapor from MODIS, *IEEE Trans. Geosci. Remote Sens.*, *41*, 442–458.

Kleespies, T. J., and L. M. McMillin (1990), Retrieval of precipitable water from observations in split window over various surface temperatures, *J. Appl. Meteorol.*, *29*, 851–862.

Knabb, R. D., and H. E. Fuelberg (1997), A comparison of the first-guess dependence of precipitable water estimates from three techniques using GOES data, *J. Appl. Meteorol.*, *36*, 417–427.

LAADS (2007), The Level 1 and Atmosphere Archive and Distribution System, Goddard Distributed Active Archive Center (http://ladsweb.nascom.nasa.gov/data).

Li, Z., J.-P. Muller, and P. Cross (2003), Comparison of precipitable water vapor derived from radiosonde, GPS, and Moderate-Resolution Imaging Spectroradiometer measurements, *J. Geophys. Res.*, *108*(D20), 4651, doi:10.1029/2003JD003372.

Li, Z., J.-P. Muller, P. Cross, P. Albert, J. Fischer, and R. Bennartz (2006), Assessment of the potential of MERIS near-infrared water vapour products to correct ASAR interferometric measurements, *Int. J. Remote Sens.*, *27*, 349–365.

Mallet, C., E. Moreau, L. Casagrande, and C. Klapisz (2002), Determination of integrated cloud liquid water path and total precipitable water from SSM/I data using a neural network algorithm, *Int. J. Remote Sens.*, *23*, 661–674.

Met Office (2006), UK Meteorological Office, Met Office-Global Radiosonde Data, [http://badc.nerc.ac.uk]. British Atmospheric Data Centre [2006], Available from http://badc.nerc.ac.uk/data/radiosglobe/.

Motell, C., J. Porter, J. Foster, M. Bevis, and S. Businger (2002), Comparison of precipitable water over Hawaii using AVHRR-based split-window techniques, GPS and radiosondes, *Int. J. Remote Sens.*, *23*, 2335–2339.

NCSA (2003), *HDF Reference Manual*, HDF Version 4.2 Release 0. National Center for Supercomputing Applications (NCSA) at the University of Illinois. Copyright 1988-2003 The Board of Trustees of the University of Illinois, 605 E. Springfield Ave. Champaign, IL 61820-5518, Illinois.

Ottlé, C., and C. François (1999), Further insights into the use of the split-window covariance technique for precipitable water retrieval, *Remote Sens. Environ.*, *69*, 84–86.

Ottlé, C., S. Outalha, C. François, and S. Le Maguer (1997), Estimation of total atmospheric water vapor content from split-window radiance measurements, *Remote Sens. Environ.*, *61*, 410–418.

Pacione, R., E. Fionda, R. Ferrara, R. Lanotte, C. Sciarretta, and F. Vespe (2002), Comparison of atmospheric parameters derived from GPS, VLBI and a ground-based microwave radiometer in Italy, *Phys. Chem. Earth*, *27*, 309–316.

Prince, S. D., and S. N. Goward (1995), Global net primary production: A remote sensing approach, *J. Biogeogr.*, *22*, 2829–2849.

Prince, S. D., S. J. Goetz, R. O. Dubayah, K. P. Czajkowski, and M. Thawley (1998), Inference of surface and air temperature, atmospheric precipitable water and vapor pressure deficit using Advanced Very High-Resolution Radiometer satellite observations: comparison with field observations, *J. Hydrol.*, 212–213, 230–249.

Ricchiazzi, P., S. Yang, C. Gautier, and D. Sowle (1998), SBDART: A research and teaching software tool for plane-parallel radiative transfer in the Earth's atmosphere, *Bull. Am. Meteorol. Soc.*, *79*, 2101–2114.

Roger, J. C., and E. F. Vermote (1998), A method to retrieve the reflectivity signature at 3.75 μm from AVHRR data, *Remote Sens. Environ.*, *64*, 103–114.

Rousseeuw, P. J. (1984), Least median of squares regression, *J. Am. Stat. Assoc.*, *79*, 871–880.

Rousseeuw, P. J., and A. M. Leroy (1987), *Robust regression and outlier detection*, John Wiley & Sons, Inc., New York.

Rousseeuw, P. J., and K. Van Driessen (2000), An algorithm for positive-breakdown regression based on concentration steps, in *Data Analysis: Scientific Modeling and Practical Application*, edited by W. Gaul, O. Opitz and M. Schader, Springer-Verlag, New York, 335–346.

Schroedter-Homscheidt, M., A. Drews, and S. Heise (2007), Total water vapor column retrieval from MSG-SEVIRI split window measurements exploiting the daily cycle of land surface temperatures, *Remote Sens. Environ (In Press, Corrected Proof, Available online)*.

Smith, W. L. (1991), Atmospheric soundings from satellites—False expectation or the key to improved weather prediction?, *Q. J. R. Meteorol. Soc.*, *117*, 267–297.

Sobrino, J. A., Z.-L. Li, M. P. Stoll, and F. Becker (1994), Improvements in the split-window technique for land surface temperature determination, *IEEE Trans. Geosci. Remote Sens.*, *32*, 243–253.

Thai, S., and M. V. Schonermark (1998), Determination of the column water vapor of the atmosphere using backscattered solar radiation measured by the Modular Optoelectronic Scanner (MOS), *Int. J. Remote Sens.*, *19*, 3223–3236.

Thome, K. J., B. M. Herman, and J. A. Reagan (1992), Determination of precipitable water from solar transmission, *J. Appl. Meteorol.*, *31*, 157–165.

Uspensky, A. B., and G. I. Scherbina (1996), Derivation of precipitable water from METEOR and NOAA infrared window measurements, *Adv. Space Res.*, *18*, 17–20.

Walpersdorf, A., M.-N. Bouin, O. Bock, and E. Doerfinger (2007), Assessment of GPS data for meteorological applications over Africa: Study of error sources and analysis of positioning accuracy, *J. Atmos. Sol. Terr. Phys.*, *69*, 1312–1330.

Xoplaki, E., J. F. González-Rouco, D. Gyalistras, L. Luterbacher, R. Rickli, and H. Wanner (2003), Interannual summer air temperature variability over Greece and its connection to the large-scale atmospheric circulation and Mediterranean SSTs 1950–1999, *Clim. Dyn.*, *20*, 537–554.

N. Chrysoulakis, Y. Kamarianakis, and Z. Mitraka, Foundation for Research and Technology–Hellas (FORTH), Institute of Applied and Computational Mathematics, Vassilika Vouton, P.O. Box 1358, 71110, Heraklion, Crete, Greece. (zedd2@iacm.forth.gr)

J. Ding and L. Xu, Chengdu University of Information Technology, Institute for Space Information and Nonlinear Sciences, Atmospheric Radiation & Satellite Remote Sensing Laboratory, Renmin South Rd. 3rd Block #3, Chengdu, Sichuan, 610041, China.